

Generative deep learning improves reconstruction of global historical climate records

Zhen Qian^{1,2}, Teng Liu^{1,2,3*}, Sebastian Bathiany^{1,2}, Shangshang Yang^{1,2}, Philipp Hess^{1,2}, Nils Bochow^{2,4}, Christian Burmester¹, Maximilian Gelbrecht^{1,2}, Brian Groenke², Niklas Boers^{1,2,5*}

¹Munich Climate Center and Earth System Modelling Group, Department of Aerospace and Geodesy, TUM School of Engineering and Design, Technical University of Munich, Munich, 80333, Germany.

²Potsdam Institute for Climate Impact Research, Potsdam, 14473, Germany.

³School of Systems Science and Institute of Nonequilibrium Systems, Beijing Normal University, Beijing, 100875, China.

⁴Alfred Wegener Institute Helmholtz Centre for Polar and Marine Research, Potsdam, Germany.

⁵Department of Mathematics and Global Systems Institute, University of Exeter, Exeter, UK.

*Corresponding author(s). E-mail(s): teng.liu@tum.de; n.boers@tum.de;

Abstract

Accurate assessment of anthropogenic climate change relies on historical instrumental data, yet observations from the early 20th century are sparse, fragmented, and uncertain [1, 2]. Conventional reconstructions rely on disparate statistical interpolation, which excessively smooths local features and creates unphysical artifacts, leading to systematic underestimation of intrinsic variability and extremes [3–5]. While recent machine learning approaches have improved reconstruction accuracy, they remain confined to purely spatial inpainting of coarse-resolution fields [6, 7]. Here, we present a unified, probabilistic generative deep learning framework that overcomes these limitations and reveals previously unresolved historical climate variability back to 1850. Leveraging a learned generative prior of Earth system dynamics, our model performs probabilistic inference to recover spatiotemporally consistent historical temperature and precipitation fields from sparse observations. Our approach preserves the higher-order statistics of climate dynamics, transforming reconstruction into a robust uncertainty-aware assessment. We demonstrate that our reconstruction overcomes pronounced biases in widely used historical reference products, including those underlying IPCC assessments, especially regarding extreme weather events. Notably, we uncover higher early 20th-century global warming levels compared to existing reconstructions, primarily driven by more pronounced polar warming, with mean Arctic warming trends exceeding established benchmarks by 0.15–0.29 °C per decade for 1900–1980. Conversely, for the modern era, our reconstruction indicates that the broad Arctic warming trend is likely overestimated in recent assessments, yet explicitly resolves previously unrecognized intense, localized hotspots in the Barents Sea and Northeastern Greenland. Furthermore, based on our seamless global reconstruction that recovers precipitation variability across the oceans and under-monitored regions, we uncover an intensification of the global hydrological cycle. Our results provide a globally complete, uncertainty-aware, spatiotemporally consistent temperature and precipitation reconstruction back to 1850, enabling more precise assessments of historical anthropogenic climate change, especially with regard to historical changes in extreme weather events, even in the polar regions where observations are sparse.

1 Introduction

Understanding historical climate change is crucial for constraining the climate system's current state and predicting its future trajectory [1, 8, 9]. However, our view of historical climate change remains incomplete. Instrumental measurements of essential variables, such as temperature or precipitation, only extend back to the early 19th century at best, and are restricted to a highly limited number of observation sites [4, 10]. Even with the introduction of satellite observations in the 1970s, many regions remain poorly observed [11, 12]. Accurate knowledge of the evolution of temperature and precipitation is fundamental to understanding Earth's energy and water cycles [13, 14] as well as past changes of climate variability and extreme events, yet observational gaps obscure the pace of long-term warming, the dynamics of climate variability, and the occurrence of past extremes [15]. Reconstructing climate fields is therefore indispensable, turning sparse data into spatiotemporally consistent records that underpin assessments of variability, change, and budget analyses [16, 17].

A variety of techniques have been developed to reconstruct climate fields. Statistical approaches, such as Gaussian processes, Kriging, and angular-distance weighting (ADW), exploit spatial covariance to interpolate across missing regions, and have been shown to be effective in producing long-term pixel-wise datasets [18]. These methods are used to create global gridded benchmark datasets such as HadCRUT5 [4] and Berkeley Earth [19], which form the basis for the United Nations Intergovernmental Panel on Climate Change (IPCC) Sixth Assessment Report (AR6) [9]. However, it is well recognized that these interpolation methods inherently prioritize minimizing error variance, often at the cost of suppressing high-frequency variability and spatial heterogeneity [1, 20–22]. By smoothing over data-sparse regions, such approaches tend to dampen the magnitude of local extremes and smear distinct climatic gradients [15, 19]. Consequently, while robust for diagnosing large-scale mean states, such conventional interpolations inevitably compress the dynamic range of historical climate, placing a conservative lower bound on the climate system's intrinsic variability.

More recently, deterministic machine-learning approaches have offered promising alternatives. Convolutional inpainting models, including partial convolutional networks [6] and Fourier-domain architectures [7], can capture finer spatial patterns. However, those methods largely remain confined to coarse-resolution (e.g., 5°) temperature fields and formulate reconstruction as a static spatial inpainting problem, thereby neglecting the evolving dynamics of the climate system through time. Such temporal consistency is particularly important for representing dynamical properties such as autocorrelation and variance, which underpin analyses of stability changes of potential tipping systems [23–28].

Generative machine learning offers a fundamental departure from these deterministic approaches. Unlike standard deterministic inpainting models, which must be trained on specific input-mask pairs and often struggle to generalize to the irregular sparsity of historical records, generative models learn to approximate the complex high-dimensional probability distribution underlying the physical system in an unsupervised manner [29, 30]. Among these models, probabilistic diffusion models (DMs) have emerged as the method of choice, overcoming the training instabilities and mode collapse that are characteristic of generative adversarial networks (GANs) [31–33]. By integrating spatiotemporal neural architectures, DMs can approximate the joint high-dimensional distribution of evolving dynamical systems in space and time, effectively learning the unconditional prior distribution of the climate states [34–37]. This capacity enables DMs to reconstruct the temporal continuity of climate fields, explicitly capturing dependencies [38] that are often neglected by the static spatial interpolation used in current methods [6, 7]. Crucially, the score-based formulation [39] facilitates controllable conditional generation, allowing DMs to flexibly integrate sparse observations as constraints to ensure that reconstructions are spatiotemporally consistent, physically plausible, and faithful to historical records [36, 38, 40].

Here, we present a generative, DM-based probabilistic framework to improve the structural limitations of primary gridded observational products of global temperature and precipitation (Supplementary Fig. S1; see Methods and Supplementary Notes for details), as used in the IPCC's assessment reports. In this framework, we unconditionally pre-train a DM to encode the joint spatiotemporal distribution of Earth system dynamics, derived from historical climate model simulations and reanalysis data. Subsequently, the model employs sparse observations as dynamical constraints to guide the generation of complete climate fields. Leveraging this pre-trained model, we introduce two complementary reconstruction modes by adjusting the sampling steps during the generation process. First, DM-Fid (Fidelity) utilizes extensive sampling steps to resolve intricate fine-scale dynamics

and structural details in space and time, making it ideal for investigating regional climate variability and localized extremes. Second, DM-Ens (Ensemble) utilizes shorter steps to efficiently generate large ensembles, facilitating the probabilistic assessment of global trends and uncertainties, such as global mean temperature changes. As demonstrated in both synthetic and realistic evaluation experiments, our reconstructions of temperature and precipitation substantially improve existing, state-of-the-art reconstructions especially regarding extremes. Our framework overcomes the limitations of interpolation artifacts, restoring critical nuances in historical climate evolution that have previously been obscured. Our results indicate an underestimation of early 20th-century polar warming in standard products, suggesting that recovering intrinsic variability is key to reconciling these discrepancies. Moreover, our reconstruction improves the representation of modern Arctic warming without inflating the regional trend, while resolving small regions with intense warming that are absent from existing gridded products. Beyond global temperature, we provide a complete reconstruction of global precipitation, including over the historically unobserved ocean, confirming a robust, century-scale intensification of the hydrological cycle. Collectively, these results provide a globally complete, uncertainty-aware temperature and precipitation reconstruction from 1850 to present, offering a refined empirical foundation for assessing historical anthropogenic climate change and Earth system stability, as well as an improved high-resolution reference for Earth system models and emerging AI models [31, 41–45].

2 Results

2.1 Generative reconstruction of climate dynamics

We first evaluate our generative reconstruction framework using synthetic test cases, benchmarking its performance against the state-of-the-art LaMa deep learning model [7] and widely used statistical methods (Kriging [4] for temperature and ADW [3] for precipitation). The evaluation experiments are conducted at resolutions corresponding to key IPCC AR6 reference datasets: 5° and 1° for temperature (HadCRUT5, Berkeley Earth) and 0.5° for precipitation (CRU TS 4.09 [3], GPCC v2022 [46]).

Evaluation of temperature reconstruction

For global temperature reconstructions, our framework demonstrates robust capability in accurately recovering coherent climate patterns even from a coverage of observations of only 5%, when assuming random coverage. Conditioned on these 5% of temperature observations, both DM variants successfully recover high-amplitude, large-scale anomalies (Fig. 1a and Supplementary Fig. S2a). This includes strong warm anomalies over the Arctic and North Africa (Supplementary Fig. S3a,b), as well as pronounced cold anomalies over northern Eurasia (Supplementary Fig. S3c). Notably, DM-Fid recovers structurally coherent anomalies even in completely unobserved regions, such as the broad cool signal across North America (Supplementary Fig. S3d), as it leverages temporal continuity and global teleconnection structures [47] learned during pre-training.

In contrast, benchmark methods exhibit pronounced structural limitations. Kriging produces strongly oversmoothed fields. LaMa correctly identifies the broad geographical placement of anomalies, but consistently underestimates their intensity, particularly in data-sparse regions (e.g., Pacific and Atlantic Oceans in Fig. 1a). Furthermore, LaMa overall fails in the higher resolution cases — 1° temperature reconstruction (Supplementary Fig. S2a). Likely because its convolutional architecture is optimized for natural image inpainting [48], it does not explicitly capture the fine-scale texture and higher-order statistical characteristics of high-resolution climate fields.

This fidelity extends to the temporal domain, where our generative approach consistently outperforms deterministic baselines across diverse climatic regions (Fig. 1b and Supplementary Fig. S2b and S4). Local time-series analysis shows that the DM reconstructions maintain high phase coherence and amplitude accuracy, resulting in the lowest errors and closely tracking the monthly evolution. In contrast, benchmark methods show substantial discrepancies: LaMa consistently underestimates the amplitude of anomalies, while Kriging systematically suppresses variability due to smoothing, leading to substantial pixel-wise deviations from the ground truth (Supplementary Fig. S4e).

Moving to a holistic spatiotemporal assessment, we observe that the disparity in reconstruction fidelity amplifies as observations become scarcer (Fig. 1c and Supplementary Table S1). As measured by global temporal coherence (mean temporal correlation coefficient) and spatial accuracy (mean spatial normalized root mean square error; see Methods), our framework significantly outperforms benchmark methods across all sparsity levels. In regimes of extreme sparsity, the DM-Ens yields

the most robust metrics, leveraging averaging of multiple ensemble members to suppress stochastic fluctuations and maintain stability.

Evaluation of precipitation reconstruction

Compared to temperature, precipitation reconstruction poses a distinct challenge due to its extreme intermittency in both space and time, and its non-Gaussian statistics. Here, our generative method shows particular advantages, recovering the full spectrum of spatial and statistical variability, including heavy tails and fine-scale structures, that are systematically damped by all benchmark methods (Fig. 2). Even at 0.5° resolution with extremely sparse coverage (1% observations), both DM variants reconstruct physically coherent features of the hydrological cycle, such as the tropical rain belt. Conversely, LaMa outputs are dominated by structural noise, likely because its fast Fourier convolution design misrepresents the non-Gaussian nature of precipitation as high-frequency texture. The statistical ADW method exhibits characteristic geometric artifacts, appearing as radial “clusters” in Fig. 2a.

The advantages of generative inference are further highlighted in the tropical Hovmöller diagrams (Fig. 2b). The DM-Fid successfully captures both the magnitude and the spatial structure of large-scale climate modes, most notably resolving the intense 2010–2012 La Niña event. In contrast, ADW suffers from severe over-smoothing; although it roughly locates the anomaly centers, it underestimates the amplitude of such extreme events and fails to reproduce the fine-scale variability seen in the ground truth.

Further statistical analyses confirm our framework’s ability to accurately reproduce the full probability distribution of precipitation, including the long tails that represent extreme events, which the benchmark models fail to capture (Fig. 2c,d,e, and Supplementary Table S1). Although the ADW baseline roughly captures large-scale precipitation patterns, it systematically underestimates the peak intensity of the zonal mean precipitation and truncates the heavy tails representing extreme events (Fig. 2c,d). Spatial power spectrum analysis reveals that, while ADW accurately resolves large-scale variability, it exhibits a characteristic energy deficit at finer scales (e.g., wavelengths < 200 km) due to interpolation artifacts (Fig. 2e). In contrast, our DM approach preserves a considerably larger fraction of the high-frequency energy required to represent realistic precipitation patterns.

To isolate the mechanisms underlying the performance of our method, we conduct sensitivity analyses on the model’s core components. First, we demonstrate the necessity of the spatiotemporal architecture: while spatial-only baselines (e.g., LaMa) and standard DMs operate on static snapshots, our analysis confirms that the explicit integration of temporal information is critical. Performance improves progressively as temporal information is added, confirming that high-fidelity reconstruction requires modeling the climate as a continuous dynamical system (Supplementary Fig. S5). Second, we identify a critical role for pre-training: the model achieves a better representation of the climate dynamics when pre-trained on a hybrid dataset of CMIP6-class Earth System Model (ESM) simulations and reanalysis, compared to reanalysis alone (Supplementary Table S2). This suggests that the large-scale, physically diverse training data from ESMs effectively complements the historical record, resulting in more accurate reconstructions. Nevertheless, reanalysis data are necessary to constrain the model to observations, as relying solely on simulations could introduce systematic biases [49, 50].

2.2 Assessing reconstruction of dynamics with a real-world observation network

To evaluate our generative framework under realistic historical conditions, we apply it to a held-out CMIP6 historical simulation (CESM2 r5i1p1f, resampled to a 5° spatial resolution and excluded from training; see Methods) using a time-evolving mask that reproduces the sparse and heterogeneous coverage of the HadCRUT5 observational network [4, 7]. This approach provides a controlled evaluation scenario with the observational coverage like in the real world, but with a known ground truth. Data availability varies strongly in both space and time, with missing ratios exceeding 90% during the 19th century. The historical network is dominated by land stations and ship tracks, leaving most oceanic and polar regions unobserved for extended periods (Fig. 3a,b). This pronounced spatial and temporal heterogeneity requires the model to reconstruct fields across extensive data voids. Failing to resolve these unobserved regions, especially oceans and polar regions early in the 20th century, would introduce systematic biases into estimates of global trends, variability, and extremes.

We evaluate the reconstructions based on two critical criteria: spatial accuracy and the preservation of temporal dynamics. In data-void regions, our DM fundamentally alters the error landscape.

The DM-Fid reconstruction achieves a spatially weighted mean absolute error (MAE) of 0.06, compared with 0.16 for LaMa and 0.12 for Kriging (Fig. 3c). Error maps reveal a strong reduction of the large positive biases characteristic of the benchmark methods, particularly over the polar regions and the Southern Ocean, where observations are most limited. These improvements stem from the model's ability to propagate information over time and through learned dynamical relationships also over long distances.

Temporal fidelity is evaluated via four widely used higher-order statistics, which are sometimes also used as indicators of changing stability [23, 25, 51, 52]: the lag-one autocorrelation (AC1), variance, skewness, and kurtosis. AC1 reflects short-term memory, variance measures fluctuation amplitude, while skewness and kurtosis describe the frequency and intensity of extremes. The DM reproduces all four metrics with high accuracy (Fig. 3d, Supplementary Fig. S6). It shows a global mean absolute AC1 bias of 0.01, nearly three to four times lower than LaMa (0.03) and Kriging (0.04). This is particularly pronounced in polar regions, where conventional methods systematically underestimate stability (i.e., yield artificially inflated AC1). Other metrics are also captured well: variance (bias 0.06 vs. 0.23 and 0.47), skewness (bias 0.04 vs. 0.08 and 0.13), and kurtosis (bias 0.09 vs. 0.20 and 0.78) all show relatively low biases. Crucially, the preservation of these higher-order indicators is robust to changing observation density. While baseline biases surge during the data-sparse early 20th century, our method maintains consistently low errors across the entire historical timeline (Supplementary Fig. S7). In the context of accelerating climate change, such precise reconstruction of statistical indicators provides a foundation for robust assessments of climate-system resilience and emerging tipping risks, information that cannot be obtained from conventionally infilled datasets [53].

At the global scale, the ensemble configuration (DM-Ens) resolves a long-standing sampling bias in the estimation of Global Mean Temperature (GMT). GMT estimates constrained by realistic HadCRUT5 coverage patterns (masked ground truth in Fig. 3e,f) exhibit systematic biases (e.g., a warm bias historically and a cool bias in recent decades), driven by sparse observations in polar and oceanic regions [15]. Our reconstruction corrects this, yielding GMT residuals closer to the ground truth than the “masked” baseline and benchmark methods. This demonstrates that the generative ensemble actively corrects for the representational bias inherent in the instrumental record.

We extend this temporal evaluation to precipitation using the sparse station coverage of the GPCC dataset (Supplementary Figs. S8 and S9e,f). The ADW benchmark collapses to climatology wherever observations are absent, eliminating natural variability and failing to represent the underlying temporal dynamics. In contrast, our framework reconstructs coherent variability across all indicators, recovering the dynamical structure that traditional methods systematically suppress. Consequently, ADW exhibits consistently higher errors and biases, with a variance bias twice as large as in our reconstruction (Supplementary Fig. S8a–e). This confirms the improved capability of our generative method to characterize precipitation dynamics and capture extreme events. Moreover, the DM-Ens provides an improved way to quantify uncertainty: The predicted ensemble spread reliably brackets the ground-truth evolution of global land-mean precipitation, even on decadal time scales (Supplementary Fig. S8f,g).

2.3 Reconstructing historical temperature and precipitation fields

We apply our generative framework to reconstruct four key IPCC AR6 reference datasets: global temperature anomalies (HadCRUT5, Berkeley Earth) and land precipitation anomalies (CRU TS 4.09, GPCC v2022). For this, we use DMs trained at 5° and 1° spatial resolutions for the temperature data, and at 0.5° spatial resolution for the precipitation data. Specifically, we tailor the reconstruction strategy to the distinct properties of each dataset during the generation phase (Methods). This adaptation allows us to recover spatiotemporally consistent global fields that alleviate potential dynamical biases (Sec. 2.2).

Reconstruction of global surface temperature

Our reconstruction recovers complex spatial structures that are systematically smoothed out in the official products considered as benchmarks (Fig. 4a). Specifically, it generates high-amplitude anomalies over the data-void Arctic and Antarctic regions (HadCRUT5) and infers sharp regional variations (Berkeley Earth) that are otherwise diluted by interpolation. Quantitatively, this superior fidelity is confirmed by consistently lower MAE at observation sites (Supplementary Fig. S10a,b), a direct result of treating sparse observations as strict constraints rather than soft targets subject to attenuation.

When aggregated to GMT, the ensemble mean derived from DM-Ens reconstructions shows long-term agreement with official infilled records (correlations > 0.95), yet suggests crucial nuanced differences (Fig. 4b). While our HadCRUT GMT estimate aligns closely with the official product, the reconstruction of Berkeley Earth indicates a consistently higher GMT. This divergence likely stems from the “dilution effect” of traditional Kriging-based methods, which homogenize large spatial fields [1, 5]. By preserving localized warm anomalies rather than smoothing them out, our results suggest that historical global warm extremes (e.g., heat waves) may have been more intense than previously indicated by smoothed observational products.

As illustrated in Fig. 4c, comparisons with official baselines confirm the broad long-term warming trend, yet reveal a distinct divergence during the data-sparse era (e.g., 1850–1950). During this period, our DM-Fid reconstruction estimates a larger spatial extent of hot extremes (> 95 th percentile relative to 1991–2020), but a smaller extent of cold extremes (< 5 th percentile) than official infilled HadCRUT5 and Berkeley Earth products. This discrepancy diminishes as observational density increases (post-1950s), suggesting that the divergence stems from differences in how data sparsity is handled. To identify the mechanism driving this divergence, we analyze the spatial standard deviation using raw observations as a proxy for natural variability (Supplementary Fig. S11). A systematic variance deficit is identified in the official infilled products, e.g., median spatial standard deviation of 0.86°C (official infilled) vs. 1.13°C (raw sparse observations) and 1.30°C (our reconstruction) for HadCRUT5. This confirms that the statistical interpolation methods used (e.g., Gaussian processes and Kriging) artificially suppress spatial heterogeneity. By generating physically plausible high-frequency signals, our approach enables hot anomalies to exceed extreme thresholds that would otherwise be smoothed out. Conversely, in the data-sparse 19th century, the official products exhibit widespread, spatially uniform cold extremes. Such patterns can also be attributed to the smoothing effect of statistical interpolation: Given that the 19th-century mean state is generally colder than the modern baseline, interpolating without simulating intrinsic variability tends to keep vast continuous areas below the cold extreme threshold. In contrast, our reconstruction introduces greater natural variability during the data-sparse early 20th century in time and space, thus reducing the total area classified as extremely cold.

Leveraging our method’s enhanced ability to capture unobserved extremes, we investigate the long-term evolution of the El Niño–Southern Oscillation (ENSO). Crucially, our reconstruction corroborates all events detected by official baselines while nearly doubling the number of identified historical El Niño events. These recovered El Niño events, which are all documented in historical synthesis (refs. [54–56]; Supplementary Fig. S12a), are largely absent in the HadCRUT5 and Berkeley Earth official infilled datasets. This advantage is most pronounced during the data-sparse period from 1900 to 1920. Notably, our model recovers a robust signal for the 1918–1919 event. This result supports the findings of ref. [57], who argued that the intensity of this El Niño was historically underestimated in standard records due to the sparse observations available during World War I. This improved detection is supported by the recovery of coherent spatial structures, leveraging teleconnections (Supplementary Fig. S12b). Unlike the diffuse signals in official products, our reconstruction resolves the canonical “bull’s tongue” pattern of warming that extends across the equatorial Pacific, demonstrating the model’s ability to localize intense thermodynamic anomalies, even in data-sparse eras. Furthermore, our probabilistic approach explicitly quantifies reconstruction uncertainty (grey shading in Supplementary Fig. S12a), providing essential context for interpreting these early 20th-century fluctuations.

Reconstruction of global land precipitation

We condition the DM on sparse land station data (CRU TS 4.09 and GPCC v2022) at the 0.5° spatial resolution to generate plausible precipitation anomalies across the entire globe, including the unobserved oceans (Fig. 5a). This represents a unique advance over ADW-based official infilled products, which are strictly limited to continental regions. At regional scales (e.g., Africa, South America, China, Siberia, and Canada in Fig. 5b and Supplementary Fig. S13), the DM-Fid reconstruction replaces the characteristic “geometric artifacts” and smoothing of the official products with physically realistic, localized storm patterns. Validation of raw station observations of CRU TS and GPCC confirms that this improved texture translates to substantially lower reconstruction errors (Supplementary Fig. S10c,d).

The inferred oceanic precipitation is a purely “out-of-sample” reconstruction generated via learned teleconnections. We evaluate this against the Global Precipitation Climatology Project (GPCP) [11], an independent satellite-based dataset that provides precipitation observations over both land and

ocean for the modern era (1981–2020) (Supplementary Fig. S14). The reconstructed trends show a correlation of $r = 0.25$ across the global ocean (see Supplementary Fig. S14c,e for correlations of trend patterns stratified by signal-to-noise ratios). For reference, the ERA5 reanalysis, which directly assimilates satellite observations, yields a correlation of $r = 0.49$ against GPCP. This indicates that even without direct oceanic inputs, our method correctly captures the major modes of hydroclimatic variability.

While the DM-Ens ensemble mean captures interannual global land mean precipitation (LMP) variability consistently with official records (Fig. 5c), a divergence appears in the spatial coverage of wet extremes (>95 th percentile relative to 1991–2020) prior to 1950 (Fig. 5d,e). To diagnose the physical origin of this discrepancy, we examine the spatial variance of precipitation anomalies in two regions classified using auxiliary station-count metadata (Fig. 5d,e and Supplementary Fig. S11b). In station-supported regions, where observations are available, official products also show a variance deficit relative to our reconstruction, reflecting the smoothing inherent in interpolation-based methods. This variance deficit becomes extreme in station-free regions: CRU TS 4.09 collapses toward near-zero variance, where it is filled by climatology, while GPCC v2022 exhibits strongly damped variability. Because these statistical reconstructions lack the spatial texture needed to populate the distribution tails, they systematically underestimate the spatial extent of early-20th-century wet extremes. Our results, therefore, suggest that these wet events were substantially more widespread than reported by official infilled products.

2.4 Informing climate assessments

To assess the large-scale climate change indicators emphasized in the recent IPCC AR6 (Working Group I, Chapter 2) [9], we re-evaluate global temperature and precipitation trends using the four latest authoritative gridded datasets (i.e., HadCRTU5, Berkeley Earth, CRU TS 4.09, and GPCC v2022) and our respective reconstructions. We investigate signals that are likely obscured by observational sparsity or methodological limitations.

Re-evaluating historical temperature trends

During the data-sparse pre-satellite era (1900–1980), our reconstruction provides a spatially complete global temperature trend analysis (Fig. 6a and Supplementary Fig. S15a). Crucially, our reconstructed fields are accompanied by explicit pixel-wise uncertainty quantification (Fig. 6b and Supplementary Figs. S15b and S16). The trend uncertainty analysis identifies regions of lower confidence (e.g., polar regions), caused by limited observations, while emphasizing robust signals elsewhere. This spatially continuous view suggests potential climate variability that is not captured in official infilled observational baselines, most notably indicating a broad, high-amplitude warming signal over the Arctic (Fig. 6c and Supplementary Fig. S15c). While the lack of historical ground truth in this region precludes definitive validation, our results highlight a considerable divergence from official products. Quantitatively, when calculated as the area-weighted average of statistically significant trends (dashed lines in Fig. 6d and Supplementary Fig. S15d), our reconstructions yield a global warming rate that exceeds official infilled baselines by 0.02 ± 0.001 °C (HadCRUT5) to 0.05 ± 0.003 °C (Berkeley Earth) per decade (values represent mean ± 1 s.d.). This difference is primarily driven by the Arctic, where our reconstruction infers warming trends that surpass official estimates by 0.15 ± 0.001 °C (HadCRUT5) and 0.29 ± 0.012 °C (Berkeley Earth) per decade.

The structural cause of this discrepancy is further elucidated by the statistical distribution of trends (Fig. 6d). Official temperature products exhibit trend distributions that are notably shifted toward lower magnitudes in the Arctic, a characteristic likely attributable to the systematic bias of interpolation methods in data-sparse regions. We investigate this hypothesis using a controlled experiment on held-out CMIP6 simulations with realistic historical observation masks (Supplementary Fig. S17). In this synthetic setting, where the ground truth is known, Kriging interpolation (a standard method for official infilled products) indeed results in a distinct negative shift of the probability density function, systematically underestimating the central tendency of the warming rate (Supplementary Fig. S17b). In contrast, our DM reconstruction accurately recovers the distribution profile of the CMIP6 ground truth. This suggests that the higher-magnitude warming distributions recovered in our historical analysis (dark red lines in Fig. 6d) may offer a more physically plausible representation of 20th-century climate evolution, effectively mitigating the damping artifacts associated with traditional interpolation.

In the satellite era (1981–2024), a period of comprehensive instrumental coverage, the global mean temperature trends of our reconstruction align closely with official products (indicated by overlapping dashed lines in upper panels in Fig. 6d and Supplementary Fig. S15d). However, substantial differences emerge in local-scale heterogeneity, particularly pronounced in the Arctic. While official infilled products often present warming as broad, smooth gradients, our approach resolves the distinct local structure of temperature change. We validate this spatial structural fidelity over the Arctic using independent remotely sensed surface temperature data (AVHRR Polar Pathfinder, APP) and reanalysis (ERA5) (Supplementary Figs. S18 and S19). Our reconstruction achieves consistently higher pixel-level spatial correlations with these references compared to official products (Supplementary Figs. S18b and S19b). This divergence highlights the smoothing artifacts inherent in statistical interpolation, which tend to suppress spatial heterogeneity in data-sparse regions. Consequently, official infilled products of HadCRUT5 and Berkeley Earth likely inflate trends in the observation-restricted interior by extrapolating strong warming signals from coastal margins. This interpolation artifact results in an overestimation of the mean Arctic warming trend, exceeding our estimate by 0.10 ± 0.002 °C (HadCRUT5) and 0.07 ± 0.011 °C (Berkeley Earth) per decade (Fig. 6d and Supplementary Fig. S15b).

While inflating the regional mean, this smoothing simultaneously suppresses pixel-level extremes, most notably along the Arctic periphery (e.g., the Barents Sea). In the Barents Sea zone, official HadCRUT5 and Berkeley Earth products dampen the warming signal, capping the maximum local amplification factor (ratio of pixel-wise to global mean trend [58]) at approximately 5, with spatial 95th percentiles reaching 4.6 (Supplementary Figs. S20a and S21a). In contrast, our reconstruction recovers the intensity of this warming signal, resolving maxima exceeding 7 (ensemble spatial 95th percentiles: 5.2–6.0). This magnitude aligns with the localized rapid-warming structure captured by ERA5 but substantially exceeds the damped estimates from official products. Validation against stations confirms this better fidelity across the Arctic, where our reconstruction outperforms both official infilled products at over 70% of sites (Supplementary Table S3 and Supplementary Fig. S22). Particularly in high-sensitivity regions (e.g., Northeast Greenland and the Barents Sea), our reconstruction preserves strong warming signals that are otherwise systematically masked by the smoothing effects of interpolation.

Based on these findings, we further identify a critical nuance in Arctic Amplification assessments. While our reconstruction yields a lower estimate, official infilled products and ERA5 reanalysis both estimate a higher Arctic Amplification factor (approximately 3.2, Supplementary Fig. S23). Our analysis suggests that this agreement is likely coincidental: Official products appear to overestimate the mean by spuriously inflating trends in the data-sparse Arctic interior due to smoothing, while ERA5 exhibits a systematic warming bias ($+0.05$ °C dec $^{-1}$) against the raw, non-infilled in-situ observations used in HadCRUT5 and Berkeley Earth (Supplementary Figs. S20b and S21b).

Re-evaluating historical precipitation trends

We further assess global precipitation trends to investigate the evolution of the hydrological cycle between the historical pre-satellite period (1901–1980) and the modern satellite era (1981–2020). Unlike gauge-based products (CRU TS 4.09 and GPCC v2022), which are restricted to terrestrial domains, our generative framework provides a globally complete assessment of precipitation change, strongly exploiting global atmospheric teleconnection structures (Fig. 6e and Supplementary Fig. S24a). Crucially, our reconstructions are accompanied by explicit uncertainty quantification (Fig. 6f and Supplementary Fig. S24b), which allows us to distinguish robust signals from regions of lower confidence, such as the tropical regions.

Focusing first on the terrestrial domain (where observational constraints exist), the statistical distribution of statistically significant trends reveals a divergence between the historical and modern periods. There is a consistent broadening of the distribution in the modern era relative to the long-term historical record (Fig. 6g, left panel; Supplementary Fig. S24c, left panel). The modern distribution (grey) is characterized by a flatter peak and significantly heavier tails compared to the historical baseline (blue). This structural shift indicates an intensification of the terrestrial hydrological cycle over land, manifesting as increasingly severe extremes, both wetting and drying, rather than a uniform shift in the mean.

Remarkably, this signal of intensification is also evident in the inferred oceanic domain. Despite being an out-of-sample inference constrained only by terrestrial observations, the oceanic trend distributions exhibit a similar, distinct broadening in the modern era (Fig. 6g, right panel; Supplementary

Fig. S24c, right panel). While historical ocean trends remain tightly clustered, the modern era reveals the widespread emergence of distinct wetting and drying patterns. The fact that our model infers this intensification over the unobserved ocean implies that the thermodynamic amplification of the hydrological cycle, characterized by increased variability and extremes, may be a robust, globally coupled feature of the recent climate [59, 60].

3 Discussion

Our probabilistic generative approach enables moving from deterministic, spatial interpolation to a spatiotemporally consistent realization of physical climate variability. By faithfully capturing climate dynamics, we reconstruct spatially seamless patterns with natural variability that inform the established baselines of historical warming. Our uncertainty-aware reconstructions of global temperature and precipitation fields outperform state-of-the-art baselines across metrics and evaluations, and exhibit several key improvements over official data products. Specifically, we infer nearly twice as many strong El Niño events as detected in official temperature products, validating our reconstruction against historical literature. Crucially, this corrective capacity extends to the poles, where our results highlight the profound uncertainty characterizing Arctic climate evolution across the entire record. During the data-sparse early 20th century (1900–1980), reconstructed trends show distinct warming that is more pronounced than in previous official infilled datasets, suggesting that these products have systematically damped historical variability. In the modern satellite era (1981–2024), we reveal that official infilled HadCRUT5 and Berkeley Earth records likely overestimate the modern Arctic warming trend due to smoothing artifacts, while simultaneously masking the intensity of localized extremes. By resolving local warming heterogeneity, we find that the widely reported four-fold Arctic Amplification [58] is likely an overestimation driven by the artificial smoothing inherent in traditional interpolation. The distinct warming patterns in the 1900–1980 and 1981–2024 periods, concentrated in regions of sea-ice retreat and coastal zones, likely reflect a response to positive albedo feedbacks and land-ocean contrasts. However, given the persistent discrepancies among reanalysis, satellite, and infilled records, a definitive ground truth remains elusive; thus, all assessments of Arctic climate evolution warrant cautious interpretation regarding their structural uncertainties.

Reconstructing precipitation poses a distinct challenge due to its localized, intermittent, and non-Gaussian statistics. Conventional interpolation methods, which revert to mean climatology in the absence of data [3], effectively erase historical variability in data-sparse regions. Our reconstructions overcome this limitation, inferring widespread drying trends in Africa and South America that are structurally missed by official datasets. This improvement is substantial as it suggests that station-based assessments, which prioritize station-supported wet regions, may overestimate the net rate of global land wetting due to a clear sampling bias: meteorological networks cluster in populated, moisture-rich zones while under-sampling arid and remote regions where drying is most pronounced. By resolving these long-standing observational gaps, our spatially complete baseline offers a more equitable evidence base for global climate policy, potentially supporting initiatives such as the UNFCCC Global Stocktake's Loss and Damage assessments in vulnerable, under-monitored regions.

Furthermore, we extend the reconstruction to the oceans, producing a global historical precipitation record inferred strictly from terrestrial inputs via learned atmospheric teleconnections. Despite being a completely “out-of-sample” inference, our model captures large-scale oceanic precipitation signals. This performance is notable given the intrinsic uncertainty of oceanic observations: even the ERA5 reanalysis in the modern satellite period, which assimilates satellite data, achieves a trend correlation of only $r = 0.49$ against GPCP, establishing an observational upper bound. Our reconstructed oceanic fields thus represent a valuable, albeit higher-uncertainty, baseline for investigating global historical hydroclimatic coupling where direct observations are lacking. To ensure appropriate caution in interpretation, we provide uncertainty maps that distinguish robust teleconnection signals from low-confidence regions, and evaluate performance across different signal-to-noise regimes (Supplementary Fig. S14c,e).

Despite these advances, many challenges remain in providing reliable, high-resolution reconstructions of historical climate data. A limitation stems from our framework's reliance on training distributions derived from climate models. While we incorporate ERA5 reanalysis to mitigate simulation biases, ERA5 itself represents a model-constrained estimation rather than the absolute ground truth of the climate system. Consequently, our reconstruction could inevitably inherit biases from these source datasets. Although our model captures physically plausible circulation patterns more

effectively than traditional statistical interpolation, it does not currently enforce strict conservation laws (e.g., mass and energy balance) during inference. This generative approach prioritizes the recovery of realistic high-frequency variability, which may result in physical inconsistencies, such as discontinuities in sea surface temperature gradients. Furthermore, while our design avoids the error accumulation endemic to traditional forecasts based on autoregressive models, it requires stitching together independent time windows, which can introduce temporal discontinuities at the boundaries (see Methods). Future work could extend the framework to a multivariate setting, integrating both learned cross-variable dependencies and explicit physical rules as constraints on the generation process. Coupled with improvements in seamless multi-decadal continuity, this approach would ensure that AI-reconstructed climate fields remain rigorously grounded in physics.

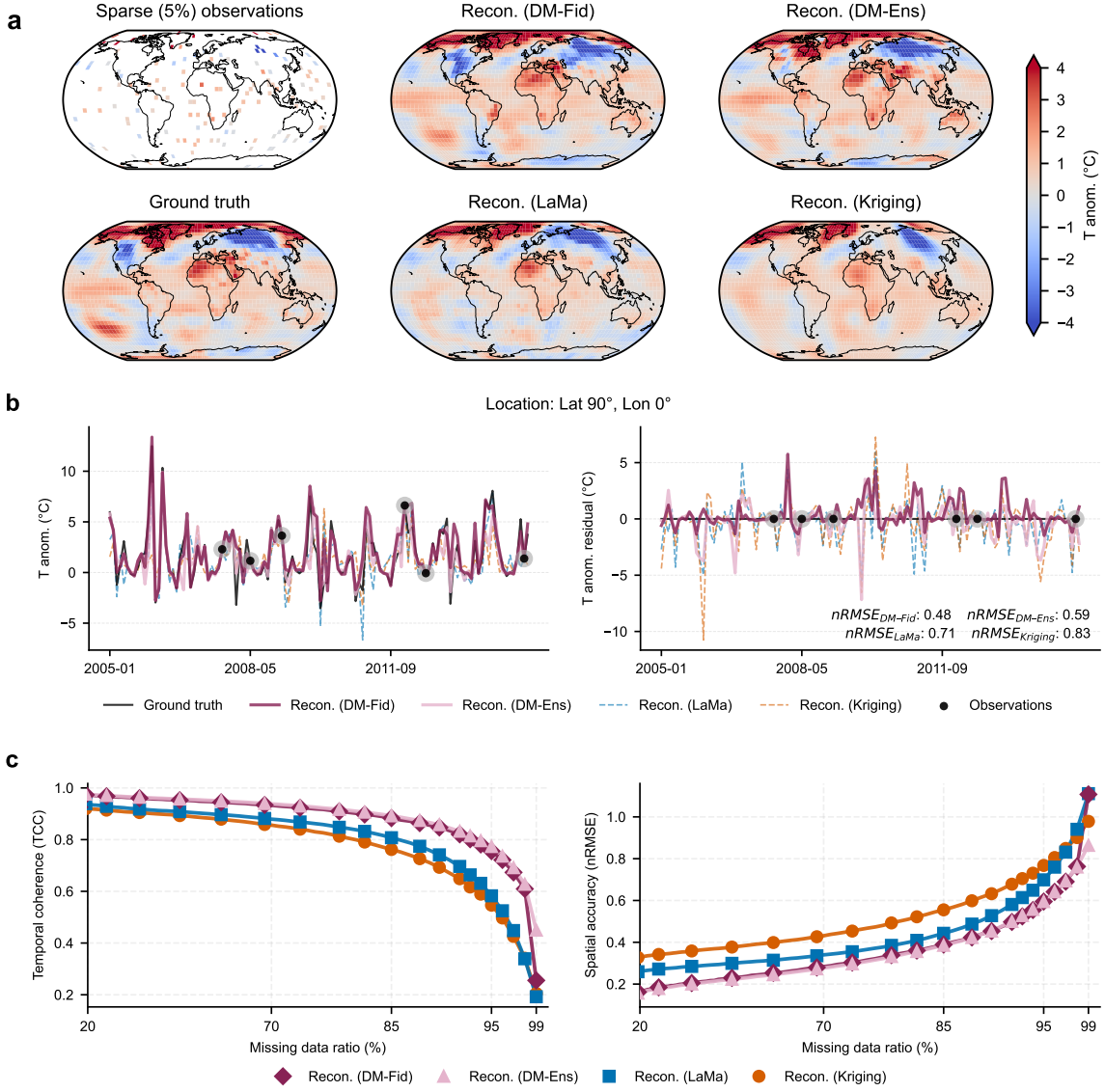


Fig. 1 Reconstruction of global temperature anomalies (5 °) from synthetic sparse input. **a**, Global snapshots of a representative monthly anomaly (ERA5 test set) reconstructed from 5% random observational coverage. The diffusion model (DM) panels display a single generated realization ($N = 1$) for both the high-fidelity (DM-Fid) and ensemble (DM-Ens) configurations, compared with deterministic baselines (LaMa, Kriging). **b**, Local analysis at a representative polar location (90°N , 0°). The left subpanel illustrates the temporal variability of the reconstruction against the ground truth, while the right subpanel displays the residual errors (reconstruction minus ground truth) for each method. For DM-Fid and DM-Ens, a single ensemble member is plotted to demonstrate the variability. Black dots indicate the sparse observational constraints available to the models. **c**, Quantitative evaluation of reconstruction accuracy as a function of data sparsity. Performance is assessed using temporal coherence (mean temporal correlation coefficient, TCC) and spatial accuracy (mean spatial normalized root mean square error, nRMSE) across varying missing-data ratios. Metrics are derived from ensemble means ($N = 5$ for DM-Fid; $N = 50$ for DM-Ens) to ensure robust comparison with deterministic baselines.

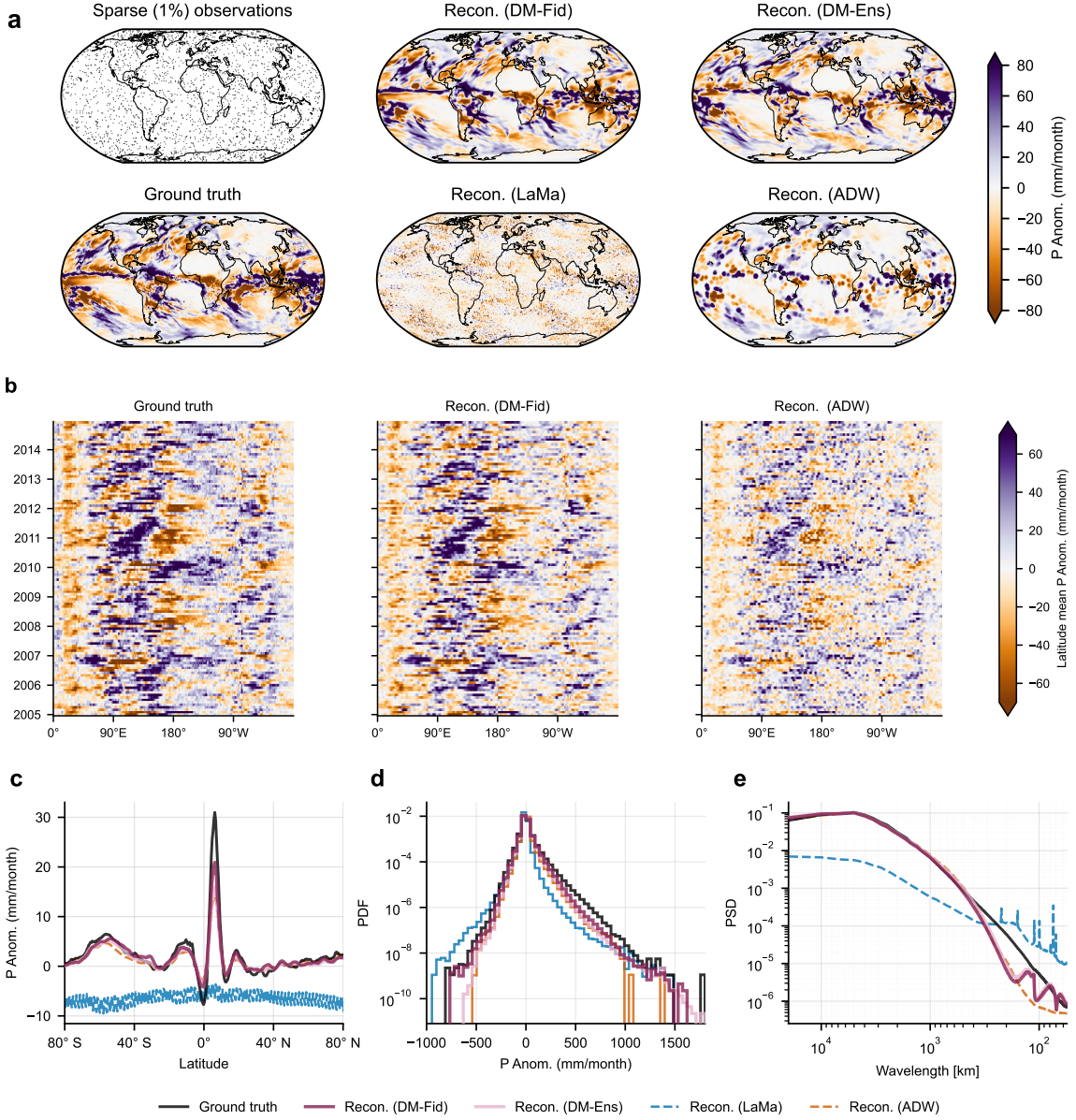


Fig. 2 Reconstruction of global precipitation anomalies (0.5 °) from synthetic sparse input. **a**, Global snapshots of a representative monthly anomaly (ERA5 test set) reconstructed from 1% random observational coverage. Maps display single-member reconstructions (DM-Fid, DM-Ens) from the generative models alongside deterministic baselines (LaMa, ADW). **b**, Hovmöller diagrams of tropical precipitation anomalies (averaged over 15°S–15°N). The comparison between Ground Truth, a single DM-Fid member, and ADW demonstrates our model’s ability to reconstruct realistic spatiotemporal variability and extreme values that are otherwise obscured by the ADW interpolation. **c**, Zonal mean of reconstructed precipitation anomalies, averaged over the full time period. **d**, Temporally averaged spatial probability density function (PDF), computed for each time step and then averaged. **e**, Temporally averaged Power Spectral Density (PSD), showing the mean energy distribution across spatial scales. In panels **c–e**, DM-Fid ($N = 5$) and DM-Ens ($N = 50$) are compared to the benchmarks.

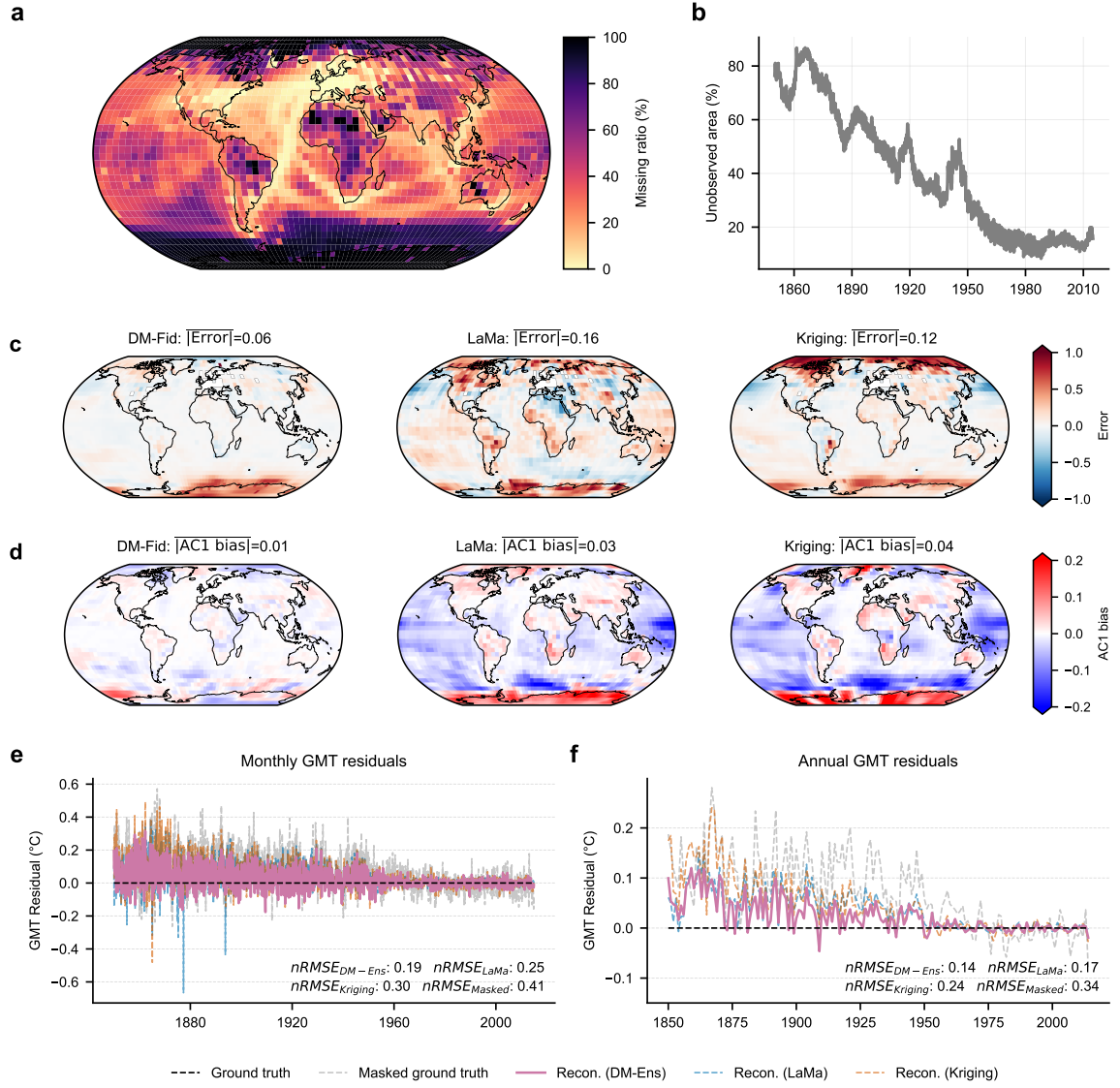


Fig. 3 Evaluation of historical reconstruction using realistic HadCRUT5 coverage. All panels use a completely held-out CMIP6 ensemble member (CESM2 r5i1p1f1, 1850–2014) as the ground truth, with masking based on the historical HadCRUT5 observational coverage. **a, b**, Spatial pattern of the time-averaged missing data ratio and its corresponding global mean temporal evolution from the HadCRUT5 mask. **c**, Time-averaged pixel-wise reconstruction error (reconstruction - ground truth) in unobserved regions for a single member of DM-Fid ($N = 1$) and the benchmark models. The global metrics denote the latitude-weighted mean absolute error (MAE). **d**, Bias in the lag-one autocorrelation (AC1), a metric for temporal memory, for DM-Fid ($N = 1$) and the benchmark models, summarized by the latitude-weighted mean absolute bias. **e, f**, Monthly and annual residuals for the reconstructed Global Mean Temperature (GMT), defined as reconstructed GMT minus ground-truth GMT. The DM-Ens reconstruction represents the average of the GMTs calculated from each of the 50 ensemble members. The “masked ground truth” represents the GMT calculated directly from the held-out CMIP6 member with the sparse observational masks, illustrating the observational coverage bias.

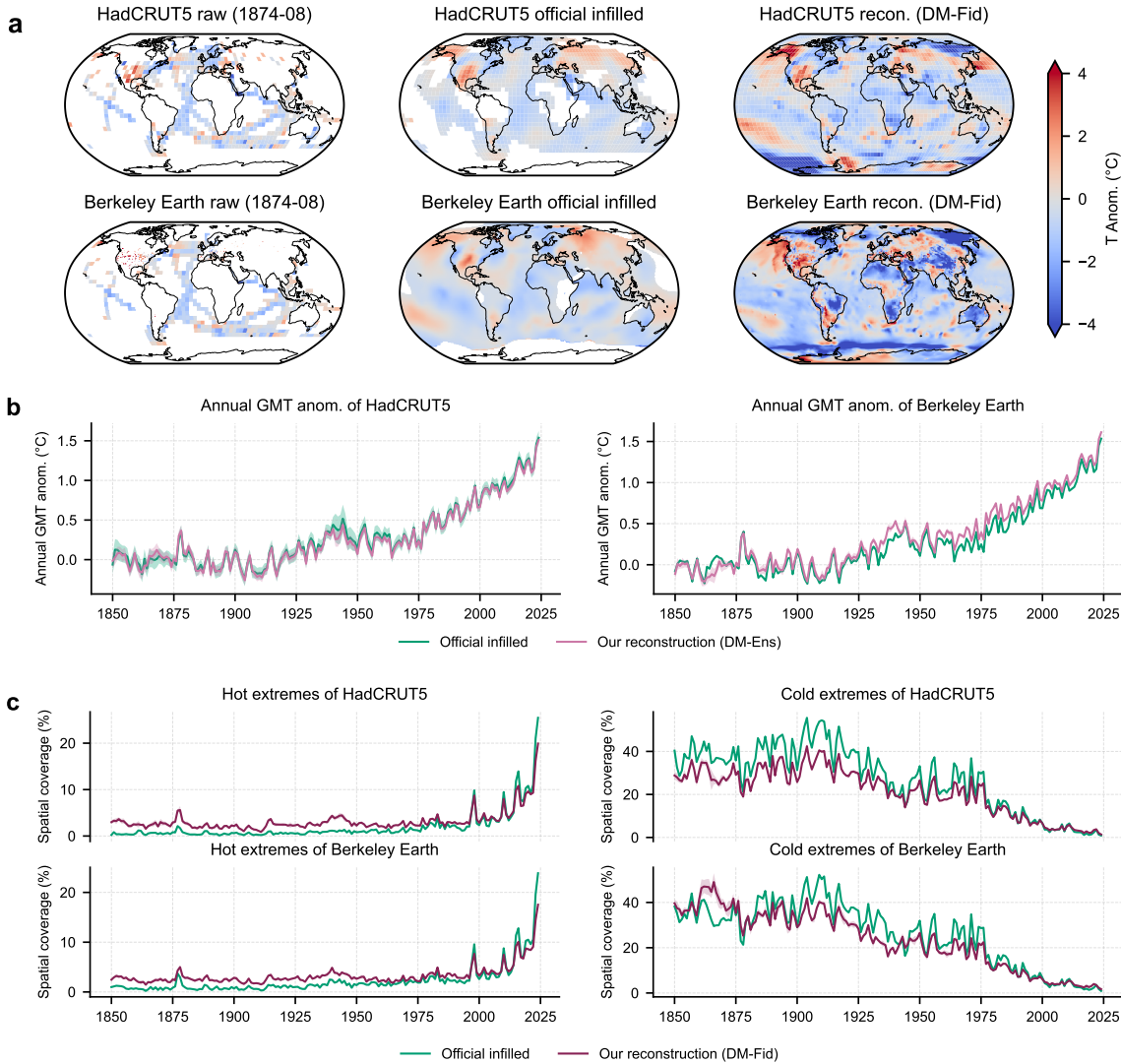


Fig. 4 Reconstruction of key global temperature datasets. **a**, Spatial comparison of a representative month (August 1874) for HadCRUT5 and Berkeley Earth. Columns display the sparse input observations (the HadCRUT5 median and the combination of HadSST 4.2 and Berkeley Earth land stations), the official infilled product, and a single DM-Fid reconstruction ($N = 1$). Note the recovery of sharp regional anomalies in the DM-Fid reconstruction compared to the smoother official baselines. **b**, Annual Global Mean Temperature (GMT) anomalies relative to the 1850–1900 pre-industrial baseline. For HadCRUT5, the reconstruction (pink) represents the mean and 95% confidence interval derived from a nested ensemble (50 DM-Ens members generated for each of the 200 observational ensemble members). For Berkeley Earth, the uncertainty is derived from 50 DM-Ens members. **c**, Evolution of the spatial coverage of temperature extremes. The DM-Fid reconstruction is presented as the mean of 5 ensemble members, with shaded regions indicating the 95% confidence interval. Hot and cold extremes are defined as the fraction of the total area with valid data where anomalies exceed the 95th or fall below the 5th percentile, respectively, of the modern reference period (1991–2020).

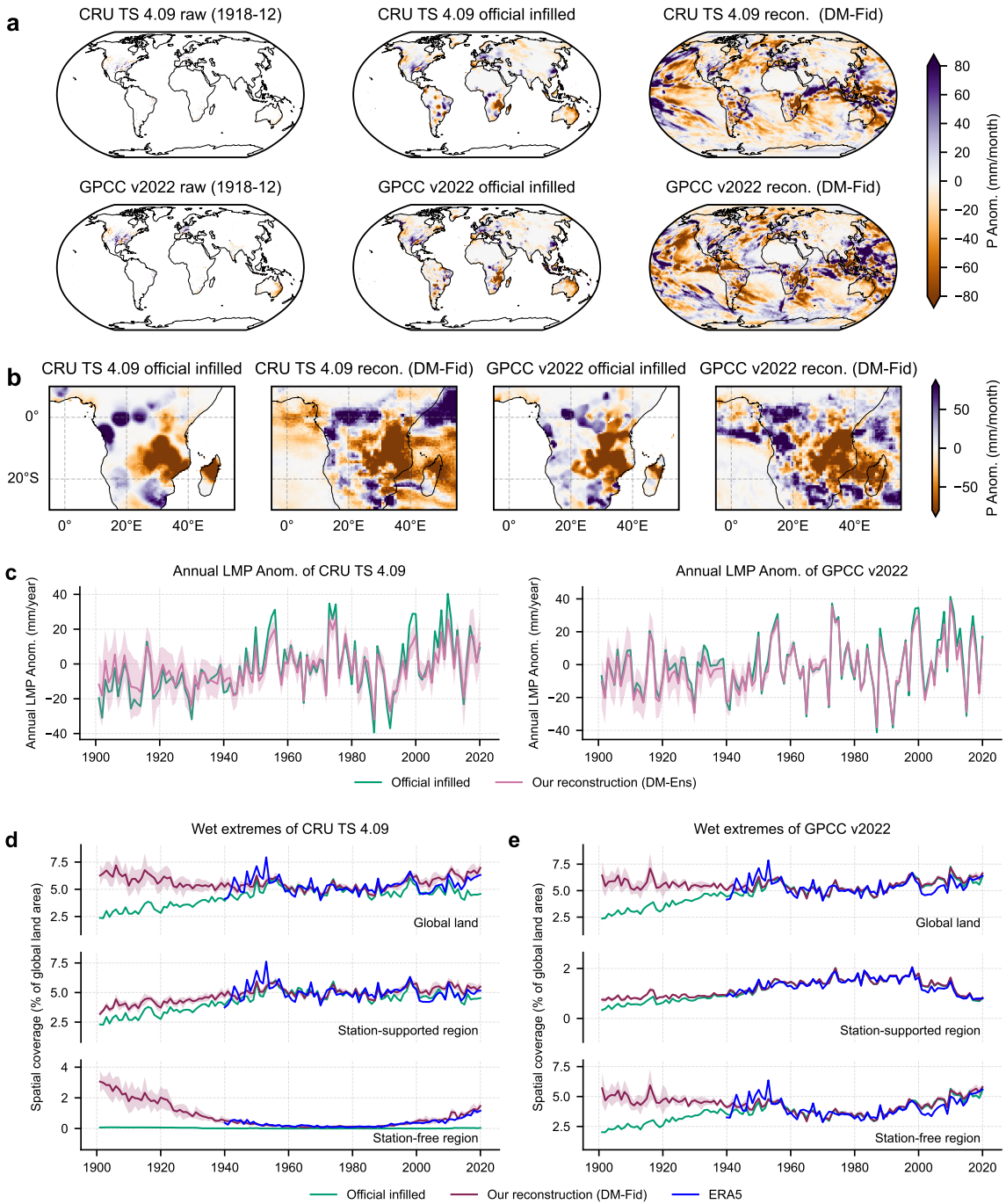


Fig. 5 Reconstruction of key precipitation datasets. **a**, Global spatial patterns of precipitation anomalies for a representative historical month (December 1918) based on CRU TS 4.09 and GPCC v2022. Columns display the sparse inputs aggregated from raw land stations, the official infilled products, and single realizations ($N = 1$) from our high-fidelity reconstruction (DM-Fid). Note that DM-Fid infers coherent oceanic precipitation structures strictly from land-based conditioning. **b**, Regional comparison over Africa highlighting the textural distinction: official products exhibit characteristic geometric artifacts (smooth radial clusters), whereas DM-Fid generates complex, physically plausible spatial structures. **c**, Annual Global Land Mean Precipitation (LMP) anomalies relative to the 1961–1990 baseline. The DM-Ens reconstruction (pink, $N = 50$) is shown as the ensemble mean with a 95% confidence interval. **d**, **e**, Evolution of the spatial coverage of wet extremes (fraction of land area exceeding the 95th percentile of the reference period) for CRU TS 4.09 (**d**) and GPCC v2022 (**e**). The DM-Fid reconstruction is presented as the mean of 5 ensemble members, with shaded regions indicating the 95% confidence interval. The divergence in the early 20th century is driven by station-free regions, where CRU TS 4.09 defaults to climatology (zero coverage), and GPCC v2022 suppresses variance, whereas DM-Fid maintains realistic variability consistent with ERA5 (blue line, post-1940).

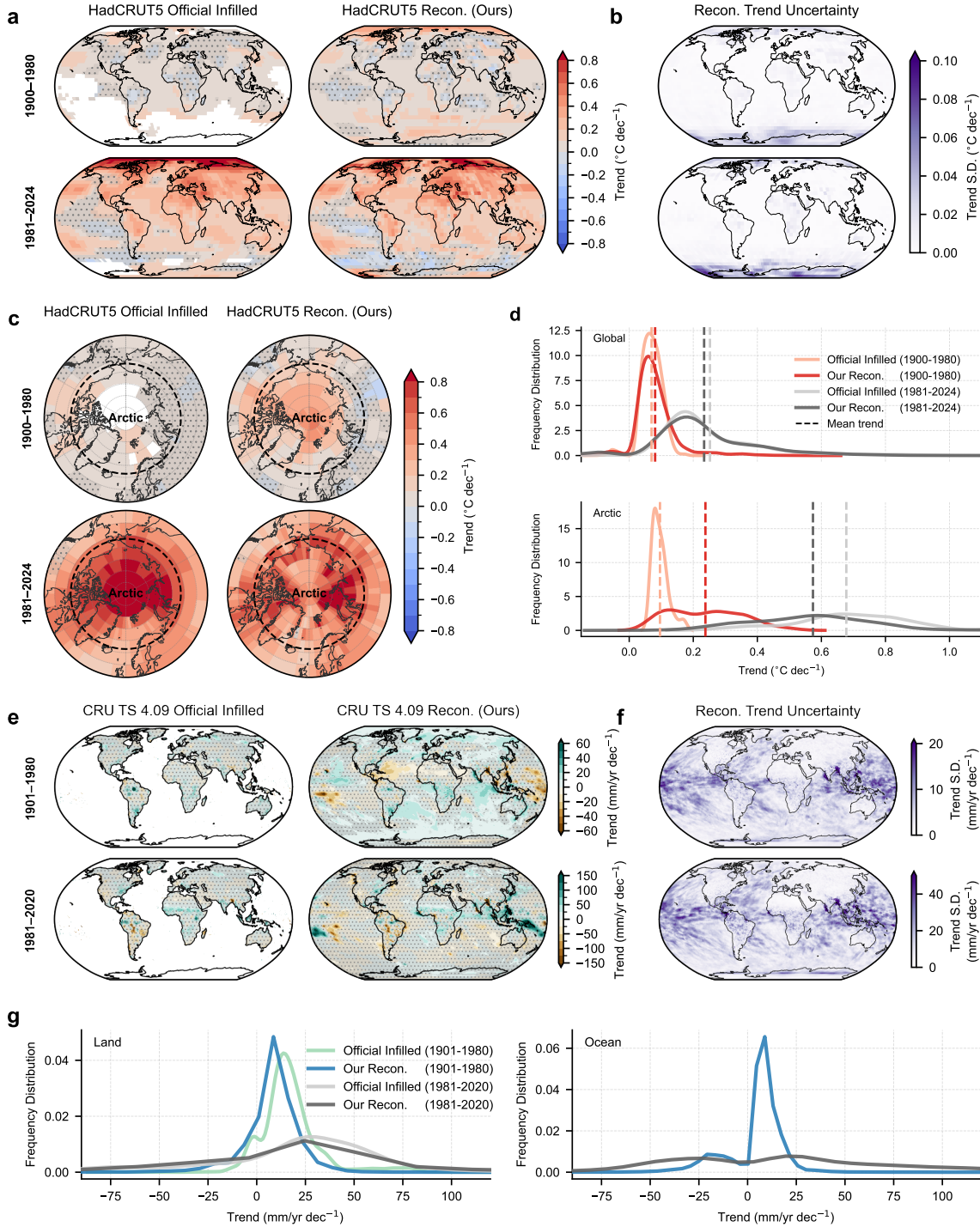


Fig. 6 Re-evaluating historical climate trends. **a**, Global linear temperature trends ($^{\circ}\text{C dec}^{-1}$) for the official infilled HadCRUT5 and our DM-Fid reconstruction (ensemble mean trend) across pre-satellite (1900–1980) and satellite (1981–2024) eras. Regions with statistically non-significant trends ($P \geq 0.05$) are masked with gray shading and stippling. Statistical significance is assessed following an AR(1) adjustment after ref.[61] to account for serial correlation. For the official infilled product, the resulting p -values are subsequently adjusted using a False Discovery Rate (FDR) control [62]. For our reconstruction, the AR(1)-adjusted p -values from the ensemble members are combined using Fisher's method, followed by an FDR correction to strictly control for false discoveries. **b**, Uncertainty of the reconstructed trends, quantified as the standard deviation of the five trend maps derived from the individual DM-Fid ensemble members. **c**, Localized temperature trends shown in **a**, highlighting the Arctic region (dashed). **d**, Frequency distribution of area-weighted statistically significant temperature trends, estimated via Gaussian kernel density estimation (KDE). Vertical dashed lines indicate the mean trend (area-weighted averaging from statistically significant trends) for each distribution. **e**, Comparison of linear precipitation trends ($\text{mm yr}^{-1} \text{dec}^{-1}$) derived from the official infilled CRU TS 4.09 and our DM-Fid reconstruction across historical (1901–1980) and modern (1981–2020) periods. Note that the official product is restricted to land, whereas our reconstruction provides a spatially complete assessment. **f**, Uncertainty of the reconstructed precipitation trends, defined as in **b**. **g**, Frequency distribution of area-weighted statistically significant precipitation trends, separated into land (constrained by observations) and ocean (out-of-sample inferred via learned teleconnections).

4 Methods

4.1 Probabilistic generative reconstruction framework

Our primary objective is to reconstruct complete historical climate fields from sparse, fragmented observations. Unlike existing approaches, which rely on deterministic, purely spatial interpolation, we frame reconstruction as a probabilistic problem: estimating the conditional distribution $p(\mathbf{x} | \mathbf{y})$ of the full climate state \mathbf{x} given sparse observations \mathbf{y} , considering the intrinsic chaos and multiscale variability of the climate system. This approach (see Supplementary Fig. S1) allows us to generate physically consistent ensembles that quantify uncertainty and preserve higher-order climate statistics.

Generative climate prior. The probabilistic reconstruction is implemented using a video diffusion model [34, 39], a generative ML method that can model the probability distribution of high-dimensional spatiotemporal data and has been shown to perform well in solving the corresponding Bayesian inverse problem (see Supplementary Note 1 for details). Adopting a spatiotemporal U-Net architecture, the DM approximates the score function $\nabla_{\mathbf{x}} \log p(\mathbf{x})$ to capture the spatiotemporal joint distribution of climate variability. We pretrain the model unconditionally on historical CMIP6 simulations and ERA5 reanalysis, enabling it to learn the complex dynamics of the Earth system independent of observation locations.

Conditional inference strategy. During reconstruction, we generate data by solving a reverse-time Stochastic Differential Equation (SDE) starting from random noise. We guide this generation process using two guidance terms to ensure the output matches historical reality while maintaining coherent spatiotemporal dynamics (see Supplementary Note 2 for details).

i. Observation constraint: At each step of the generation, we force the model to align with available station observations. We define a measurement loss \mathcal{G}_{obs} that penalizes deviations between the generated field and valid observations:

$$\mathcal{G}_{obs} = \frac{\|(\hat{\mathbf{x}}_0 - \mathbf{y}) \odot \mathbf{M}\|_F^2}{\sqrt{\|\mathbf{M}\|_1 / N_{total}}} \quad (1)$$

where \odot denotes the element-wise product, $\|\cdot\|_F^2$ is the squared Frobenius norm, $\|\mathbf{M}\|_1$ counts the number of observed points, and N_{total} is the total number of points in the grid.

ii. Temporal consistency: To reconstruct long time series without discontinuities, we generate data in overlapping windows. We enforce smoothness by minimizing the difference between the end of one window and the start of the next (\mathcal{G}_{temp}).

$$\mathcal{G}_{temp} = \sum_{i=1}^{W-1} \|\text{tail}(\mathbf{w}_i) - \text{head}(\mathbf{w}_{i+1})\|_F^2 \quad (2)$$

where $\text{tail}(\mathbf{w}_i) = \mathbf{w}_i[L - O : L]$ denotes the ending segment (last O time steps) of window i , $\text{head}(\mathbf{w}_{i+1}) = \mathbf{w}_{i+1}[0 : O]$ denotes the beginning segment (first O time steps) of the subsequent window, and O represents the temporal overlap length (e.g., $O = 2$ months).

Reconstruction products. We generate two distinct reconstruction products to serve different scientific needs. The high-fidelity (DM-Fid) mode prioritizes physical realism for dynamical analysis. DM-Fid utilizes deep sampling trajectories (e.g., 1000 steps) to generate a small ensemble (e.g., 5) that preserves climate variability and extremes. The large-ensemble (DM-Ens) mode prioritizes uncertainty quantification and statistical robustness. DM-Ens employs shorter sampling trajectories (e.g., 100 or 250 steps) across a large ensemble (e.g., 50) to deliver a statistically accurate mean estimate and a robust estimate of the spread (uncertainty).

4.2 Training data and preprocessing

The DM is trained on a comprehensive historical climate dataset, comprising both ERA5 reanalysis and CMIP6 model simulations. The training dataset contains monthly mean surface air temperature (t2m, tas) and precipitation (tp, pr) fields. CMIP6 data are from 16 historical ensemble members of the models NOAA-GFDL, CESM2, and MPI-ESM1-2-HR (1850–2014). This is complemented by ERA5 reanalysis data from 1940 to 2024, also as monthly averages.

Temperature fields are spatially interpolated to both 5° (36×72 pixels) and 1° (180×360 pixels) grids, while precipitation is interpolated to a 0.5° (360×720 pixels) grid. For each variable and spatial resolution, we then compute monthly anomalies relative to the 1961–1990 climatological baseline.

For model evaluation, the 2005–2014 period is strictly held out as a test set. To ensure a rigorous assessment of generalization to independent climate trajectories, we exclude one full CMIP6 ensemble member (CESM2 r5i1p1f1) entirely from the training data, following established evaluation practices [6, 7]. We apply a cube-root transformation to the precipitation anomalies in order to reduce the skewness of their distribution. Subsequently, all input fields are standardized by subtracting the global mean and dividing by the global standard deviation, with these statistics computed from the training set for each variable and resolution.

4.3 Benchmarking and evaluation

We benchmark our reconstruction framework using synthetic masks with varying spatial and temporal data gaps, applied to ERA5 and CMIP6 test sets, as well as a completely held-out CMIP6 ensemble member. Performance is compared against established statistical methods: Kriging for temperature [4] and angular-distance weighting (ADW) for precipitation [3], as well as a state-of-the-art deep learning baseline, LaMa [7]. To align with our ultimate goal of reconstructing key IPCC AR6 reference datasets, all benchmarks are conducted at the corresponding spatial resolutions (5° and 1° for temperature; 0.5° for precipitation).

To assess reconstruction fidelity, we employ two complementary metrics: temporal coherence and spatial accuracy. All metrics are computed exclusively on the unobserved (masked) regions to evaluate the model’s ability to infer missing information, rather than its ability to fit existing data. Let $\mathbf{Y} \in \mathbb{R}^{T \times H \times W}$ denote the ground truth and $\hat{\mathbf{Y}}$ denote the reconstructed field. The binary mask \mathbf{M} takes a value of 0 for unobserved regions and 1 for observed regions.

Temporal coherence. We quantify the temporal accuracy of the reconstruction using the mean temporal correlation coefficient (TCC). We calculate the Pearson correlation coefficient (r) between the reconstructed and ground truth anomaly time series for each individual grid cell (i, j) within the target region. The global metric is reported as the arithmetic mean of these local correlations:

$$\text{Mean TCC} = \frac{1}{\sum_{(i,j) \in \mathcal{V}} w_{i,j}} \sum_{(i,j) \in \mathcal{V}} w_{i,j} \cdot \rho(\hat{\mathbf{Y}}_{:,i,j}[\Omega_{i,j}], \mathbf{Y}_{:,i,j}[\Omega_{i,j}]) \quad (3)$$

where \mathcal{V} is the set of valid grid cells (where correlation is defined), we apply latitude weights $w_{i,j} = \cos(\phi_i)$, where ϕ_i is the latitude of grid cell (i, j) , $\Omega_{i,j}$ represents the set of time indices where the mask is zero for location (i, j) , and ρ denotes the Pearson correlation function. A higher mean TCC indicates that the model correctly captures the evolution of climate variability over time, with a theoretical maximum of 1.

Spatial accuracy. To assess the quality of the reconstructed spatial patterns, we use the spatially calculated normalized root mean square error (nRMSE). For each time step t , we compute the RMSE over the unobserved (masked) spatial domain \mathcal{S}_t and normalize it by the spatial standard deviation (σ) of the ground truth anomalies within that same region. The final metric is reported as the mean of these normalized errors across all time steps:

$$\text{Mean nRMSE} = \frac{1}{T} \sum_{t=1}^T \sqrt{\frac{\sum_{(i,j) \in \mathcal{S}_t} w_{i,j} (\hat{\mathbf{Y}}_{t,i,j} - \mathbf{Y}_{t,i,j})^2}{\sum_{(i,j) \in \mathcal{S}_t} w_{i,j}}} \frac{\sigma_w(\mathbf{Y}_{t,\mathcal{S}_t})}{\sigma_w(\hat{\mathbf{Y}}_{t,\mathcal{S}_t})} \quad (4)$$

where \mathcal{S}_t denotes the set of spatial indices (i, j) unobserved at time t , $w_{i,j}$ is latitude weights, and $\sigma_w(\cdot)$ is the weighted standard deviation calculated over those indices. This normalization ensures the error metric accounts for the varying amplitude of natural variability across seasons and regions. A lower nRMSE indicates better recovery of spatial anomalies.

4.4 Reconstruction of IPCC AR6 reference datasets

Following successful benchmarking on synthetic data, we apply our reconstruction framework to four key reference datasets that form the foundation of the IPCC AR6 report. Crucially, our approach employs a unified pre-training strategy: a single diffusion model, once trained for a specific resolution and variable (e.g., 5° temperature), is universally applicable to any reconstruction task within that domain, regardless of the missing data pattern. Consequently, we tailor only the generation phase, adapting the spatiotemporal constraints to the unique observational characteristics of each dataset.

HadCRUT5 Temperature. HadCRUT.5.0.2.0 is a widely used global temperature dataset produced by the UK Met Office Hadley Centre and the Climatic Research Unit (CRU). It combines

sea surface temperature (SST) data with land-based station temperature records and is provided as a 200-member ensemble to represent uncertainty. As the native format is a sparse grid, our objective is to generate a complete, infilled version for each ensemble member. To generate complete global reconstructions, we utilize our unified pre-trained DM based on 5° temperature. We treat the sparse grid points from each of the 200 ensemble members as specific spatiotemporal conditions during the generation phase. For every member, we generate a DM-Fid reconstruction to infer the most probable state, and a DM-Ens reconstruction to fully quantify the generative uncertainty.

Berkeley Earth Surface Temperature The Berkeley Earth Surface Temperature dataset has been developed to address potential biases in historical climate records by incorporating an extensive number of land station records. Standard approaches for the Berkeley Earth dataset typically involve interpolating extensive land station records and combining them with interpolated 5° HadSST ocean data. Following this established practice, we utilize the 1° gridded land anomalies and the 5° HadSST dataset as our observational inputs. However, we tailor our conditioning strategy to the specific goals of each reconstruction mode based on the pre-trained DM based on 1° temperature.

For the ensemble generation (DM-Ens), our primary objective is to maintain a robust estimation of the climate state by strictly preserving the original observational information. Therefore, we condition the DM on a composite 1° field containing the land data and a 1° resampling of the HadSST data. This constraint ensures the ensemble members remain faithful to the original values.

Conversely, for the high-fidelity reconstruction (DM-Fid), we aim to generate fine-detailed patterns and super-resolve the coarse marine data. Here, we employ a dual-constraint strategy, guiding the DM with the 1° land data and the native 5° ocean data simultaneously. This configuration allows the model to infer more physically plausible spatial structure over the ocean from coarse observations, thereby avoiding the blocky “checkerboard” artifacts characteristic of naive resampling.

CRU TS 4.09 Precipitation The CRU TS 4.09 is a prominent high-resolution gridded dataset for land-based climate variables, especially precipitation. Although a ready-to-use gridded product is available, we reconstruct the sparse input directly from the raw station data rather than using the distributed grid. This is necessary because the official CRU station count metadata (*stn*) incorporates a 450 km correlation decay distance inherent to their ADW interpolation scheme, which obscures the precise location of point observations. Following the methodology described in their reference paper [3], we aggregate the raw land station data onto a 0.5° grid and compute anomalies relative to the 1961–1990 climatology. To generate spatially continuous fields, we employ the pre-trained DM based on 0.5° precipitation, utilizing the resulting sparse land grid as a spatiotemporal constraint to guide the reconstruction.

GPCC v2022 Precipitation The Global Precipitation Climatology Centre (GPCC) v2022 dataset is another global land precipitation analysis, valued for its rigorous quality control. Unlike CRU, the raw station data for GPCC is not publicly available due to licensing restrictions. However, the dataset explicitly provides the number of station observations per grid cell without the influence of extensive spatial smoothing. Consequently, we can directly utilize the official infilled product by computing monthly anomalies (1961–1990 baseline) and applying a binary mask to retain only those grid cells informed by at least one station. This derived sparse anomaly field serves as the spatiotemporal constraint for our pre-trained 0.5° precipitation DM.

Declarations

Author contribution. Z.Q., T.L., and N.Boe. conceived and designed the study. Z.Q. trained the spatiotemporal diffusion model and performed the primary experiments, with input from T.L., S.B., and N.Boe. For the baselines, T.L. and Z.Q. conducted the LaMa experiments with input from N.Boc., while C.B. and P.H. conducted the standard spatial diffusion model benchmarks. Z.Q. and T.L. discussed and interpreted the results with input from all authors. Z.Q. and T.L. wrote the original draft of the manuscript. All authors contributed to the discussion and critical revision of the paper.

Competing interests. The authors declare no competing interests.

Supplementary information. Supplementary information is available for this paper.

Data availability. The observational and reanalysis datasets used in this study are publicly available from their respective repositories. HadCRUT.5.0.2.0 data can be accessed at <https://www.metoffice.gov.uk/hadobs/hadcrut5/data/HadCRUT.5.0.2.0/download.html>. Berkeley Earth Temperature data are available at <https://berkeleyearth.org/data/>. CRU TS 4.09 data are hosted at https://crudata.uea.ac.uk/cru/data/hrg/cru_ts_4.09/. GPCC v2022 precipitation data can be downloaded from https://opendata.dwd.de/climate_environment/GPCC/html/gpcc_normals_v2022_doi_download.html. GPCP precipitation data are available via the NOAA Physical Sciences Laboratory at <https://psl.noaa.gov/data/gridded/data.gpcp.html>. ERA5 reanalysis data can be downloaded from the Copernicus Climate Change Service (C3S) Climate Data Store at <https://cds.climate.copernicus.eu/datasets/reanalysis-era5-single-levels?tab=download>. CMIP6 model simulations (including ensembles from NOAA-GFDL, CESM2, and MPI-ESM1-2-HR) are available through the Earth System Grid Federation (ESGF) node at <https://esgf-data.dkrz.de/search/cmip6-dkrz/>. NOAA Climate Data Record (CDR) of AVHRR Polar Pathfinder Extended (APP-X) can be downloaded from the NOAA National Centers for Environmental Information at <https://www.ncei.noaa.gov/data/avhrr-polar-pathfinder-extended/access/nhem/>. Norwegian Arctic station observations (SN series) are available from the Norwegian Meteorological Institute (MET Norway) at <https://seklima.met.no/>. Greenland station data (DMI Report 25-08) can be retrieved from the Danish Meteorological Institute at <https://www.dmi.dk/publikationer/>.

Code availability. The code for modeling and analysis will be publicly available upon acceptance of this manuscript for publication.

Acknowledgements. T.L. acknowledges funding from the National Key R&D Program of China no.2023YFE0109000. Z.Q. acknowledges funding from the program of the China Scholarships Council (no.202306860010). N.Boe. and S.B. acknowledge funding from the Volkswagen Foundation. N.Boc. received funding from the European Union (ERC, FORCLIMA, 101044247). This is ClimTip contribution #138; the ClimTip project has received funding from the European Union's Horizon Europe research and innovation programme under grant agreement no. 101137601. The authors gratefully acknowledge the Ministry of Research, Science and Culture (MWFK) of Land Brandenburg for supporting this project by providing resources on the high performance computer system at the Potsdam Institute for Climate Impact Research.

References

- [1] Von Storch, H. *et al.* Reconstructing past climate from noisy data. *Science* **306**, 679–682 (2004).
- [2] Doblas-Reyes, F. J. *et al.* in *Linking Global to Regional Climate Change* (eds Masson-Delmotte, V. *et al.*) *Climate Change 2021: The Physical Science Basis. Contribution of Working Group I to the Sixth Assessment Report of the Intergovernmental Panel on Climate Change* 1363–1512 (Cambridge University Press, Cambridge, United Kingdom and New York, NY, USA, 2021).
- [3] Harris, I., Osborn, T. J., Jones, P. & Lister, D. Version 4 of the CRU TS monthly high-resolution gridded multivariate climate dataset. *Sci. Data* **7**, 109 (2020).
- [4] Morice, C. P. *et al.* An updated assessment of near-surface temperature change from 1850: The HadCRUT5 data set. *J. Geophys. Res.: Atmos.* **126**, e2019JD032361 (2021).
- [5] Yamamoto, J. K. Correcting the smoothing effect of ordinary kriging estimates. *Math. Geol.* **37**, 69–94 (2005).

- [6] Kadow, C., Hall, D. M. & Ulbrich, U. Artificial intelligence reconstructs missing climate information. *Nat. Geosci.* **13**, 408–413 (2020).
- [7] Bochow, N., Poltronieri, A., Rypdal, M. & Boers, N. Reconstructing historical climate fields with deep learning. *Sci. Adv.* **11**, eadp0558 (2025).
- [8] Tokarska, K. B. *et al.* Past warming trend constrains future warming in CMIP6 models. *Sci. Adv.* **6**, eaaz9549 (2020).
- [9] Gulev, S. K. *et al.* *Changing State of the Climate System. In Climate Change 2021: The Physical Science Basis. Contribution of Working Group I to the Sixth Assessment Report of the Intergovernmental Panel on Climate Change* (Cambridge University Press, 2021).
- [10] Bojinski, S. *et al.* The concept of essential climate variables in support of climate research, applications, and policy. *Bull. Am. Meteorol. Soc.* **95**, 1431–1443 (2014).
- [11] Adler, R. F. *et al.* The version-2 global precipitation climatology project (GPCP) monthly precipitation analysis (1979–present). *J. Hydrometeorol.* **4**, 1147–1167 (2003).
- [12] Kent, E. C. & Kennedy, J. J. Historical estimates of surface marine temperatures. *Annu. Rev. Mar. Sci.* **13**, 283–311 (2021).
- [13] Allen, M. R. & Ingram, W. J. Constraints on future changes in climate and the hydrologic cycle. *Nature* **419**, 224–232 (2002).
- [14] Hansen, J., Ruedy, R., Sato, M. & Lo, K. Global surface temperature change. *Rev. Geophys.* **48** (2010).
- [15] Cowtan, K. & Way, R. G. Coverage bias in the hadcrut4 temperature series and its impact on recent temperature trends. *Q. J. R. Meteorol. Soc.* **140**, 1935–1944 (2014).
- [16] Osman, M. B. *et al.* Globally resolved surface temperatures since the Last Glacial Maximum. *Nature* **599**, 239–244 (2021).
- [17] Neukom, R., Steiger, N., Gómez-Navarro, J. J., Wang, J. & Werner, J. P. No evidence for globally coherent warm and cold periods over the preindustrial Common Era. *Nature* **571**, 550–554 (2019).
- [18] Carrassi, A., Bocquet, M., Bertino, L. & Evensen, G. Data assimilation in the geosciences: An overview of methods, issues, and perspectives. *Wiley Interdiscip. Rev. Clim. Change* **9**, e535 (2018).
- [19] Rohde, R. *et al.* A new estimate of the average Earth surface land temperature spanning 1753 to 2011. *Geoinfor. Geostat.: An Overview* **1**, 1–7 (2013).
- [20] Jones, P., Osborn, T. & Briffa, K. Estimating sampling errors in large-scale temperature averages. *J. Clim.* **10**, 2548–2568 (1997).
- [21] Hofstra, N., Haylock, M., New, M. & Jones, P. D. Testing E-OBS European high-resolution gridded data set of daily precipitation and surface temperature. *J. Geophys. Res. Atmos.* **114** (2009).
- [22] Bracco, A. *et al.* Machine learning for the physics of climate. *Nat. Rev. Phys.* **7**, 6–20 (2025).
- [23] Scheffer, M. *et al.* Early-warning signals for critical transitions. *Nature* **461**, 53–59 (2009).
- [24] Boers, N., Ghil, M. & Stocker, T. F. Theoretical and paleoclimatic evidence for abrupt transitions in the Earth system. *Environ. Res. Lett.* **17**, 093006 (2022).
- [25] Boers, N. *et al.* Destabilization of Earth system tipping elements. *Nat. Geosci.* 1–12 (2025).

[26] Brovkin, V. *et al.* Past abrupt changes, tipping points and cascading impacts in the Earth system. *Nat. Geosci.* **14**, 550–558 (2021).

[27] Rietkerk, M., Skiba, V., Weinans, E., Hébert, R. & Laepple, T. Ambiguity of early warning signals for climate tipping points. *Nat. Clim. Change* 1–10 (2025).

[28] Liu, T. *et al.* Data gaps and outliers distort critical slowing down-based resilience indicators. *Sci. Adv. (accepted)* (2026).

[29] Hess, P., Drüke, M., Petri, S., Strnad, F. M. & Boers, N. Physically constrained generative adversarial networks for improving precipitation fields from Earth system models. *Nat. Mach. Intell.* **4**, 828–839 (2022).

[30] Lugmayr, A. *et al.* IEEE (ed.) *Repaint: Inpainting using denoising diffusion probabilistic models*. (ed.IEEE) *Proceedings of the IEEE/CVF conference on computer vision and pattern recognition*, 11461–11471 (IEEE, 2022).

[31] Price, I. *et al.* Probabilistic weather forecasting with machine learning. *Nature* **637**, 84–90 (2025).

[32] Hess, P., Aich, M., Pan, B. & Boers, N. Fast, scale-adaptive and uncertainty-aware downscaling of Earth system model fields with generative machine learning. *Nat. Mach. Intell.* 1–11 (2025).

[33] Aich, M., Bathiany, S., Hess, P., Huang, Y. & Boers, N. Diffusion models for probabilistic precipitation generation from atmospheric variables. *arXiv preprint arXiv:2504.00307* (2025).

[34] Ho, J. *et al.* Video diffusion models. *Adv. Neural Inf. Process. Syst.* **35**, 8633–8646 (2022).

[35] Harvey, W., Naderiparizi, S., Masrani, V., Weilbach, C. & Wood, F. Flexible diffusion modeling of long videos. *Adv. Neural Inf. Process. Syst.* **35**, 27953–27965 (2022).

[36] Li, Z. *et al.* Learning spatiotemporal dynamics with a pretrained generative model. *Nat. Mach. Intell.* **6**, 1566–1579 (2024).

[37] Srivastava, P. *et al.* Precipitation downscaling with spatiotemporal video diffusion. *Adv. Neural Inf. Process. Syst.* **37**, 56374–56400 (2024).

[38] Yang, S. *et al.* Generative assimilation and prediction for weather and climate. *arXiv preprint arXiv:2503.03038* (2025).

[39] Song, Y. *et al.* Score-based generative modeling through stochastic differential equations. *arXiv preprint arXiv:2011.13456* (2020).

[40] Chung, H., Kim, J., Mccann, M. T., Klasky, M. L. & Ye, J. C. Diffusion posterior sampling for general noisy inverse problems. *arXiv preprint arXiv:2209.14687* (2022).

[41] Bi, K. *et al.* Accurate medium-range global weather forecasting with 3D neural networks. *Nature* **619**, 533–538 (2023).

[42] Lam, R. *et al.* Learning skillful medium-range global weather forecasting. *Science* **382**, 1416–1421 (2023).

[43] Kochkov, D. *et al.* Neural general circulation models for weather and climate. *Nature* **632**, 1060–1066 (2024).

[44] Bodnar, C. *et al.* A foundation model for the Earth system. *Nature* **641**, 1180–1187 (2025).

[45] Allen, A. *et al.* End-to-end data-driven weather prediction. *Nature* **641**, 1172–1179 (2025).

[46] Schneider, U., Hänsel, S., Finger, P., Rustemeier, E. & Ziese, M. GPCC Full Data Monthly Product Version 2022 at 0.5°: Monthly Land-Surface Precipitation from Rain-Gauges built on GTS-based and Historical Data (2022). URL https://doi.org/10.5676/DWD_GPCC/FD_M

V2022_050. Global Precipitation Climatology Centre (GPCC).

- [47] Boers, N. *et al.* Complex networks reveal global pattern of extreme-rainfall teleconnections. *Nature* **566**, 373–377 (2019).
- [48] Suvorov, R. *et al.* Resolution-robust Large Mask Inpainting with Fourier Convolutions. *arXiv preprint arXiv:2109.07161* (2021).
- [49] Zelinka, M. D. *et al.* Causes of higher climate sensitivity in CMIP6 models. *Geophys. Res. Lett.* **47**, e2019GL085782 (2020).
- [50] Tian, B. & Dong, X. The double-ITCZ bias in CMIP3, CMIP5, and CMIP6 models based on annual mean precipitation. *Geophys. Res. Lett.* **47**, e2020GL087232 (2020).
- [51] Held, H. & Kleinen, T. Detection of climate system bifurcations by degenerate fingerprinting. *Geophys. Res. Lett.* **31** (2004).
- [52] Guttal, V. & Jayaprakash, C. Changing skewness: an early warning signal of regime shifts in ecosystems. *Ecol. Lett.* **11**, 450–460 (2008).
- [53] Smith, T. *et al.* Reliability of resilience estimation based on multi-instrument time series. *Earth Syst. Dyn.* **14**, 173–183 (2023).
- [54] Quinn, W. H., Neal, V. T. & Antunez de Mayolo, S. E. El Niño occurrences over the past four and a half centuries. *J. Geophys. Res.: Oceans* **92**, 14449–14461 (1987).
- [55] Yu, J.-Y. & Kim, S. T. Identifying the types of major El Niño events since 1870. *Int. J. Climatol.* **33**, 2105–2112 (2012).
- [56] Climate Prediction Center. Cold & Warm Episodes by Season. National Oceanic and Atmospheric Administration (n.d.). URL https://www.cpc.ncep.noaa.gov/products/analysis-monitoring/ensostuff/ONI_v5.php. Accessed: 2025-12-29.
- [57] Giese, B. S. *et al.* The 1918/19 El Niño. *Bull. Am. Meteorol. Soc.* **91**, 177–183 (2010).
- [58] Rantanen, M. *et al.* The Arctic has warmed nearly four times faster than the globe since 1979. *Commun. Earth Environ.* **3**, 168 (2022).
- [59] Held, I. M. & Soden, B. J. Robust responses of the hydrological cycle to global warming. *J. Clim.* **19**, 5686–5699 (2006).
- [60] Allan, R. P. *et al.* Advances in understanding large-scale responses of the water cycle to climate change. *Ann. N. Y. Acad. Sci.* **1472**, 49–75 (2020).
- [61] Santer, B. D. *et al.* Consistency of modelled and observed temperature trends in the tropical troposphere. *Int. J. Climatol.* **28**, 1703–1722 (2008).
- [62] Wilks, D. “The stippling shows statistically significant grid points”: How research results are routinely overstated and overinterpreted, and what to do about it. *Bull. Am. Meteorol. Soc.* **97**, 2263–2273 (2016).
- [63] Ho, J., Jain, A. & Abbeel, P. Denoising diffusion probabilistic models. *Adv. Neural Inf. Process. Syst.* **33**, 6840–6851 (2020).
- [64] Hyvärinen, A. & Dayan, P. Estimation of non-normalized statistical models by score matching. *J. Mach. Learn. Res.* **6** (2005).
- [65] Karras, T., Aittala, M., Aila, T. & Laine, S. Elucidating the design space of diffusion-based generative models. *Adv. Neural Inf. Process. Syst.* **35**, 26565–26577 (2022).
- [66] Efron, B. Tweedie’s formula and selection bias. *J. Am. Stat. Assoc.* **106**, 1602–1614 (2011).

Supplementary Information for “Generative deep learning improves reconstruction of global historical climate records”

Zhen Qian^{1,2}, Teng Liu^{1,2,3,*}, Sebastian Bathiany^{1,2}, Shangshang Yang^{1,2}, Philipp Hess^{1,2}, Nils Bochow^{2,4}, Christian Burmester¹, Maximilian Gelbrecht^{1,2}, Brian Groenke² and Niklas Boers^{1,2,5,*}

¹ *Munich Climate Center and Earth System Modelling Group, Department of Aerospace and Geodesy, TUM School of Engineering and Design, Technical University of Munich, Munich, 80333, Germany*

² *Potsdam Institute for Climate Impact Research, Potsdam, 14473, Germany*

³ *School of Systems Science and Institute of Nonequilibrium Systems, Beijing Normal University, Beijing, 100875, China*

⁴ *Alfred Wegener Institute Helmholtz Centre for Polar and Marine Research, Potsdam, Germany*

⁵ *Department of Mathematics and Global Systems Institute, University of Exeter, Exeter, UK*

*Corresponding authors: teng.liu@tum.de, n.boers@tum.de

Supplementary Notes

Supplementary Note 1: Formulation of the generative diffusion process

At its core, a score-based video diffusion model (DM) learns to generate global climate fields, by reversing a noise process that systematically destroys them [39, 63]. The concept can be likened to restoring a video time frame that has been gradually corrupted by white noise. The model operates based on a predefined forward process that systematically adds noise, and then trains a neural network to meticulously reverse each step, effectively restoring a clear image from the noise (the generative process). In contrast to the above example of a video time frame, it is of course not possible to recover a specific image accurately; the task is only to generate a plausible image from the distribution of all possible images, which the DM has been trained to learn.

The forward process mathematically describes the degradation, gradually perturbing a data sample $\mathbf{x}(t)$, which is a spatiotemporal window consisting of multiple consecutive climate fields, with noise over a continuous time $t \in [0, T]$. This is formalized by a stochastic differential equation (SDE) [39]:

$$d\mathbf{x} = \mu(\mathbf{x}, t)dt + g(t)d\mathbf{w} \quad (\text{S1})$$

Here, $\mu(\mathbf{x}, t)$ represents the drift term of the forward SDE, a climate field $\mathbf{x}(0)$ is progressively transformed into a sample from a simple prior distribution (e.g., Gaussian noise) at $\mathbf{x}(T)$.

The generative process is the model's primary task: to synthesize a physically plausible climate field $\mathbf{x}(0)$ starting from a random noise sample $\mathbf{x}(T)$. This is accomplished by solving the corresponding reverse-time SDE [39]:

$$d\mathbf{x} = [\mu(\mathbf{x}, t) - g(t)^2 \nabla_{\mathbf{x}} \log p_t(\mathbf{x})]dt + g(t)d\bar{\mathbf{w}} \quad (\text{S2})$$

The crucial term here is the score function, $\nabla_{\mathbf{x}} \log p_t(\mathbf{x})$, which is the gradient of the log-probability of the data at any given noise level t . Intuitively, the score acts as a guide, pointing the generation process away from improbable states and toward the complex, underlying structure of the true data distribution.

Since this score function is not known in advance, we train a time-dependent neural network, $s_{\theta}(\mathbf{x}, t)$, to approximate it. The network is optimized by minimizing a score-matching objective [39, 64], which effectively trains the model to predict scores for any given noisy input. Specifically, we train the score network $s_{\theta}(\mathbf{x}_t, t)$ to approximate the ground-truth score function $\nabla_{\mathbf{x}_t} \log p_t(\mathbf{x}_t)$ by minimizing the following loss:

$$\mathcal{L}(\theta) = \mathbb{E}_{t, \mathbf{x}_0, \mathbf{z}} \left[\left\| \sigma_t s_{\theta}(\mathbf{x}_t, t) + \mathbf{z} \right\|_2^2 \right] \quad (\text{S3})$$

where $\mathbf{x}_t = \mu_t \mathbf{x}_0 + \sigma_t \mathbf{z}$ represents the perturbed data at time t , with $\mathbf{z} \sim \mathcal{N}(\mathbf{0}, \mathbf{I})$ being the Gaussian noise, and μ_t, σ_t derived from the SDE's marginal distribution. This weighting scheme balances the magnitude of the score function across different noise scales.

To explicitly learn the joint distribution of climate fields in space and time, we employ a spatiotemporal U-Net architecture [34] for s_{θ} , a design proven effective for video generation tasks. Once trained, this score model enables the generation of novel, physically plausible climate fields by numerically solving the reverse-time SDE (Eq. S2). For this, we employ an advanced solver from the Elucidating the Design Space of Diffusion-Based Generative Models (EDM) framework [65]. This framework uses a high-order numerical scheme that combines a deterministic step with a controlled amount of stochastic noise, guiding the generation from a state of pure noise at $t = T$ back to a clean data sample at $t = 0$ while maintaining sample diversity.

Supplementary Note 2: Conditional sampling with spatiotemporal constraints

The reconstruction task is framed as a conditional generation problem, where the goal is to infer the complete climate field, \mathbf{x} , by sampling from the posterior distribution given sparse observations, \mathbf{y} :

$$\hat{\mathbf{x}} \sim p(\mathbf{x}|\mathbf{y}). \quad (\text{S4})$$

While our pretrained model has learned the prior distribution $p(\mathbf{x})$, we guide the generative process to approximate sampling from this conditional distribution. This is achieved through a spatiotemporal

guidance mechanism that updates the score function at each step of the reverse-time SDE, using external constraints without retraining the model. Formally, we apply Bayes' rule to decompose the conditional score $\nabla_{\mathbf{x}_t} \log p_t(\mathbf{x}_t|\mathbf{y})$ into the unconditional score provided by the pretrained model and the gradient of the likelihood:

$$\nabla_{\mathbf{x}_t} \log p_t(\mathbf{x}_t|\mathbf{y}) = \underbrace{\nabla_{\mathbf{x}_t} \log p_t(\mathbf{x}_t)}_{\text{Unconditional Score}} + \underbrace{\nabla_{\mathbf{x}_t} \log p_t(\mathbf{y}|\mathbf{x}_t)}_{\text{Guidance Likelihood}} \quad (\text{S5})$$

In our approach, the likelihood term $\nabla_{\mathbf{x}_t} \log p_t(\mathbf{y}|\mathbf{x}_t)$ is approximated by two specific constraint terms in space and time, modified from ref. [36, 40].

The spatial constraint enforces fidelity to the provided sparse observations. At each step in the reverse SDE, the model generates a preliminary estimate of the complete climate field, \mathbf{x}_0 . According to Tweedie's formula [40, 66], we compute the difference between this estimate and the actual observations at the locations where data exists (defined by a mask, \mathbf{M}). This is formulated as a spatial guidance, \mathcal{G}_{obs} , based on the sum of squared errors:

$$\mathcal{G}_{obs} = \frac{\|(\hat{\mathbf{x}}_0 - \mathbf{y}) \odot \mathbf{M}\|_F^2}{\sqrt{\|\mathbf{M}\|_1 / N_{total}}} \quad (\text{S6})$$

where \odot denotes the element-wise product, $\|\cdot\|_F^2$ is the squared Frobenius norm, $\|\mathbf{M}\|_1$ counts the number of observed points, and N_{total} is the total number of points in the grid.

The temporal constraint ensures a smooth and physically plausible evolution over time, a critical feature for our spatiotemporal diffusion-based framework, which processes data in overlapping temporal windows. Let \mathbf{w}_i be the i -th generated data window. The likelihood term, \mathcal{G}_{temp} , is calculated by minimizing the squared difference between the overlapping segments of consecutive windows:

$$\mathcal{G}_{temp} = \sum_{i=1}^{W-1} \|\text{tail}(\mathbf{w}_i) - \text{head}(\mathbf{w}_{i+1})\|_F^2 \quad (\text{S7})$$

where $\text{tail}(\mathbf{w}_i) = \mathbf{w}_i[L-O : L]$ denotes the ending segment (last O time steps) of window i , $\text{head}(\mathbf{w}_{i+1}) = \mathbf{w}_{i+1}[0 : O]$ denotes the beginning segment (first O time steps) of the subsequent window, and O represents the temporal overlap length (e.g., $O = 2$ months). This constraint ensures continuity across window boundaries, preventing physical discontinuities in the reconstructed time series.

Together, these losses form a composite guidance, $\mathcal{G} = \lambda_{obs}\mathcal{G}_{obs} + \lambda_{temp}\mathcal{G}_{temp}$, where λ_{obs} and λ_{temp} are scalar weights that control the influence of each constraint (see Supplementary Table S4). The gradient of this loss with respect to the generated sample, $\nabla_{\mathbf{x}}\mathcal{G}$, is then used to guide the score function at each integration step of the reverse SDE. This perturbation effectively steers the generation trajectory towards a solution that simultaneously aligns with the sparse observations and maintains temporal coherence.

Supplementary Figures

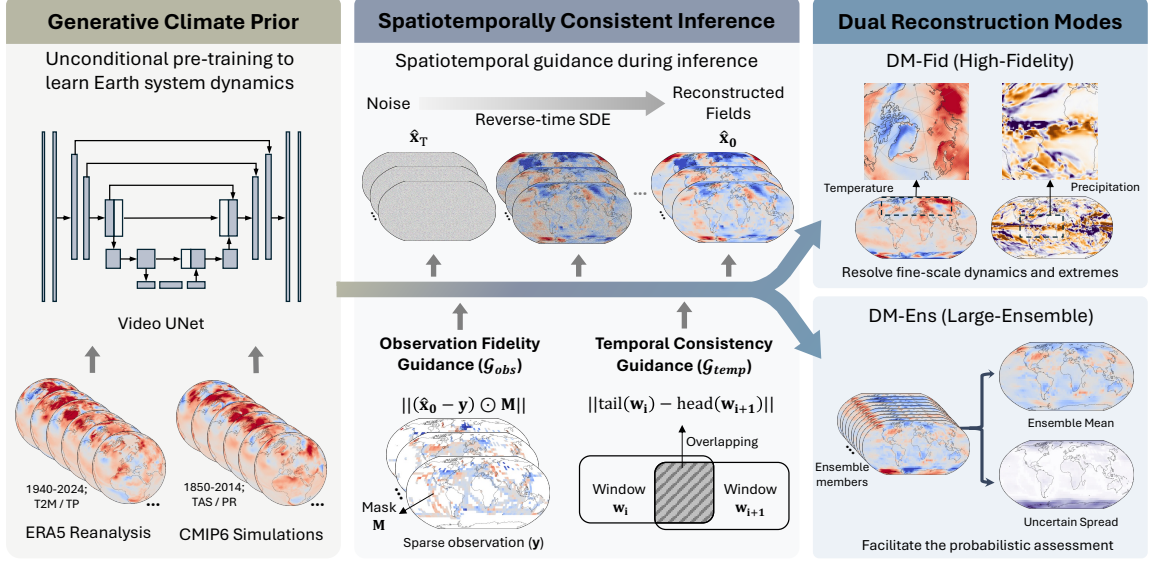


Fig. S1 Illustration of the probabilistic generative deep learning reconstruction framework. **Left**, A generative climate prior is established by unconditionally pre-training a spatiotemporal U-Net on CMIP6 simulations and ERA5 reanalysis. This allows the model to learn the joint spatiotemporal distribution of Earth system dynamics independent of historical observation locations. **Middle**, Reconstruction is performed via spatiotemporally consistent inference. The model generates climate fields by solving a reverse-time Stochastic Differential Equation (SDE) starting from noise. The generation trajectory is steered by two simultaneous gradients: Observation fidelity guidance (\mathcal{G}_{obs}), which enforces alignment with sparse station data (\mathbf{y}) at valid locations (\mathbf{M}); and temporal Consistency Guidance (\mathcal{G}_{temp}), which ensures dynamical continuity by minimizing discrepancies between the overlapping tails and heads of consecutive time windows ($\mathbf{w}_i, \mathbf{w}_{i+1}$). **Right**, This framework produces two complementary reconstruction products: DM-Fid (high-fidelity), optimized to resolve fine-scale spatial structures and extreme events; and DM-Ens (large-ensemble), which generates multiple realizations to provide an estimate of the ensemble mean and uncertainty spread.

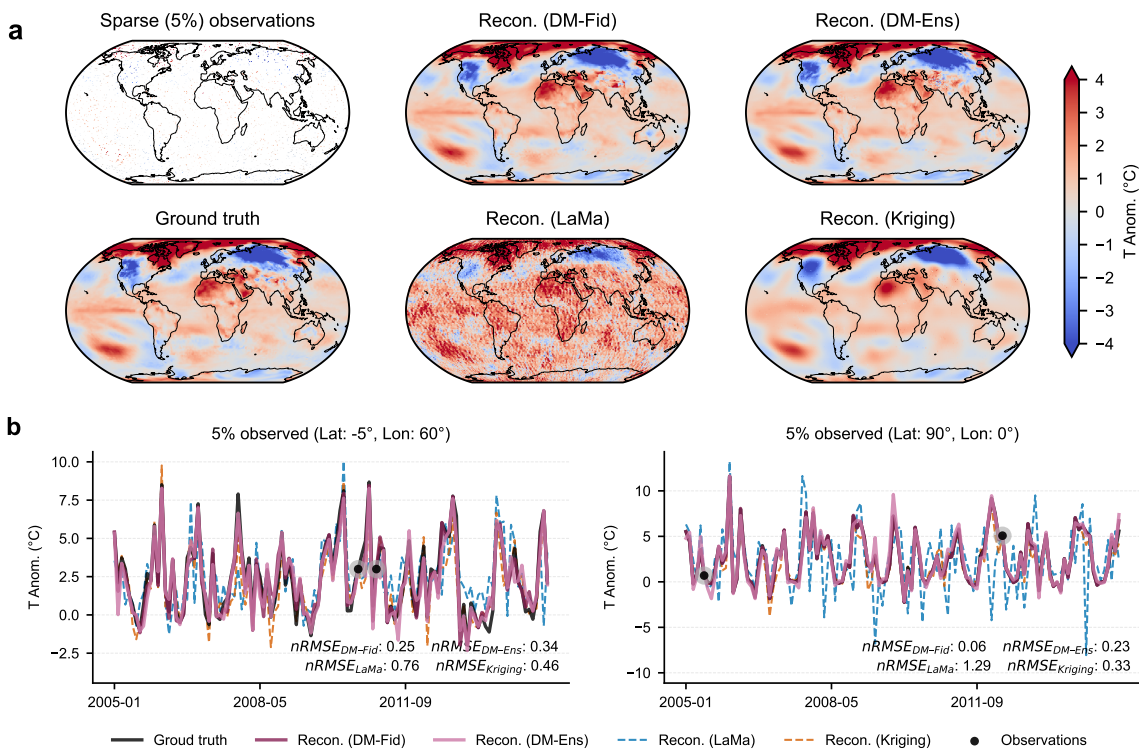


Fig. S2 High-resolution temperature reconstruction at 1° spatial resolution. **a**, Global comparison of reconstruction methods at 1° resolution given 5% observational coverage. Maps display a sample from the ERA5 test set. The generative models (DM-Fid, DM-Ens; shown as single realizations) are compared against LaMa and Kriging. Note that at this higher resolution, the smoothing effect of Kriging and the texture artifacts of LaMa are more pronounced compared to the generative approach. **b**, Local time-series analysis at tropical (5°S, 60°E) and polar (90°N, 0°) coordinates. The DM-Fid demonstrates superior variance retention compared to the baselines, preserving the amplitude of local anomalies even at fine spatial scales.

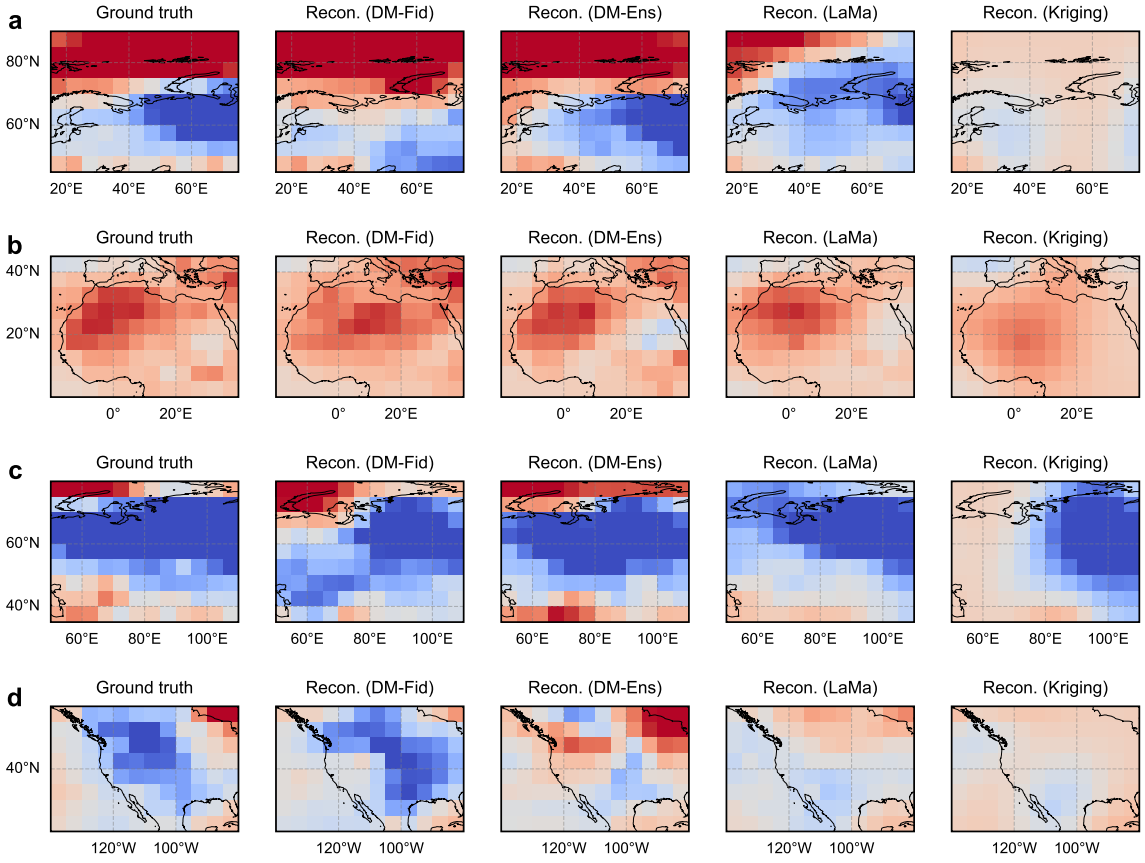


Fig. S3 Detailed regional comparison of temperature anomaly reconstruction. Zoomed-in views of representative regions from the global 5° reconstruction (Fig.1a), comparing the Ground Truth against generative models (DM-Fid, DM-Ens) and deterministic baselines (LaMa, Kriging). The color mapping is identical to that shown in Fig.1a. **a**, Arctic. **b**, North Africa. **c**, North Eurasia. **d**, North America.

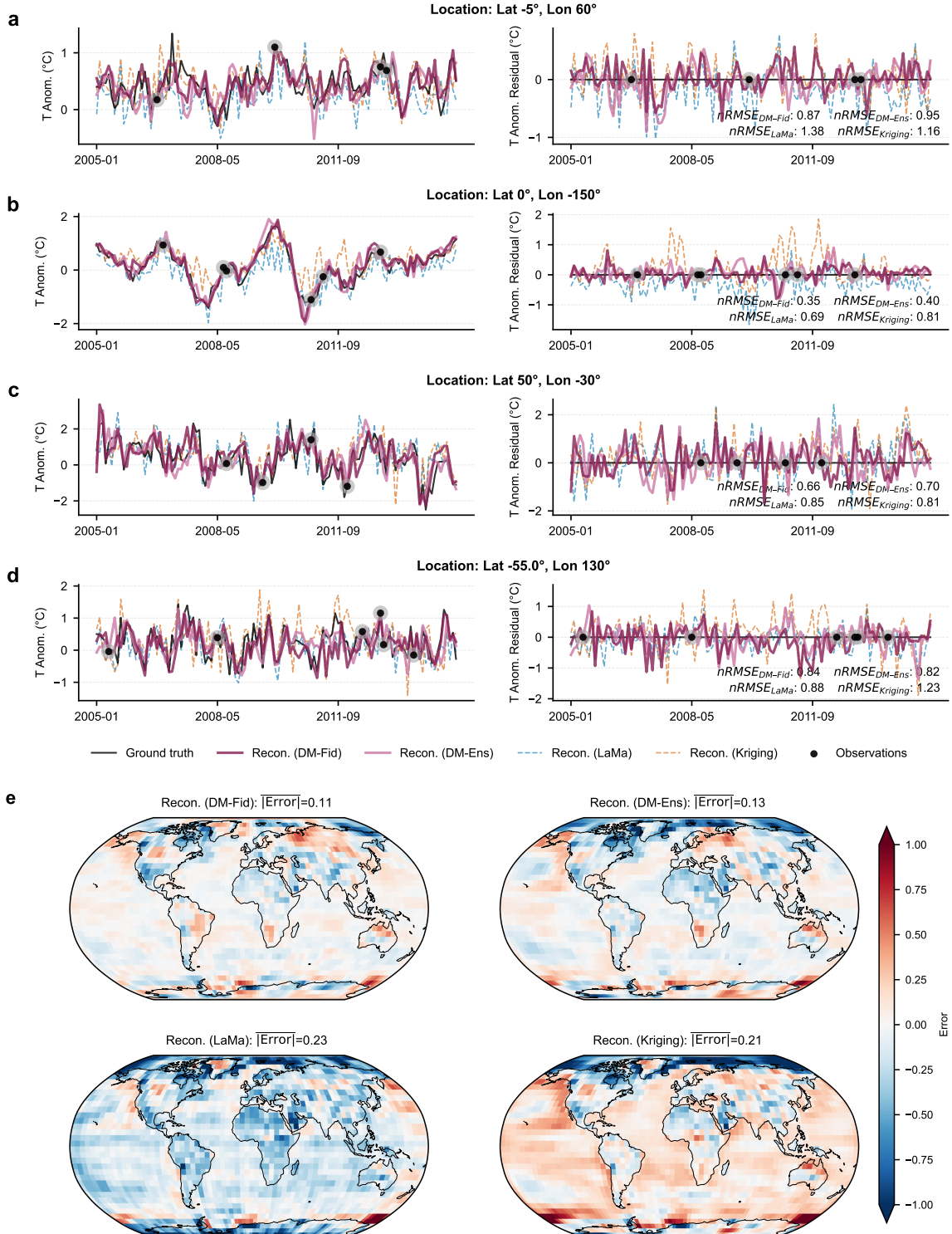


Fig. S4 Extended evaluation of reconstruction accuracy across diverse regions and global error distributions. **a-d**, Detailed local analysis at four representative locations: Tropical Indian Ocean (5°S , 60°E ; **a**), Equatorial Pacific (0° , 150°W ; **b**), North Atlantic (50°N , 30°W ; **c**), and Southern Ocean (55°S , 130°E ; **d**). Following the format of Fig. 1b, the left subpanels illustrate the temporal coherence of the reconstructions (colored lines) against the ERA5 ground truth (black line) and sparse observations (black dots). The right subpanels display the corresponding residual errors (Reconstruction – Ground Truth). **e**, Global spatial distribution of pixel-wise reconstruction error for the generative models (DM-Fid, DM-Ens) and deterministic baselines (LaMa, Kriging). The maps display the difference between the reconstructed fields and the ground truth; the value in each title ($|\bar{\text{Error}}|$) represents the globally weighted mean absolute error for the field. All results are derived from the same ERA5 test set and 5% sparse observational mask used in Fig. 1.

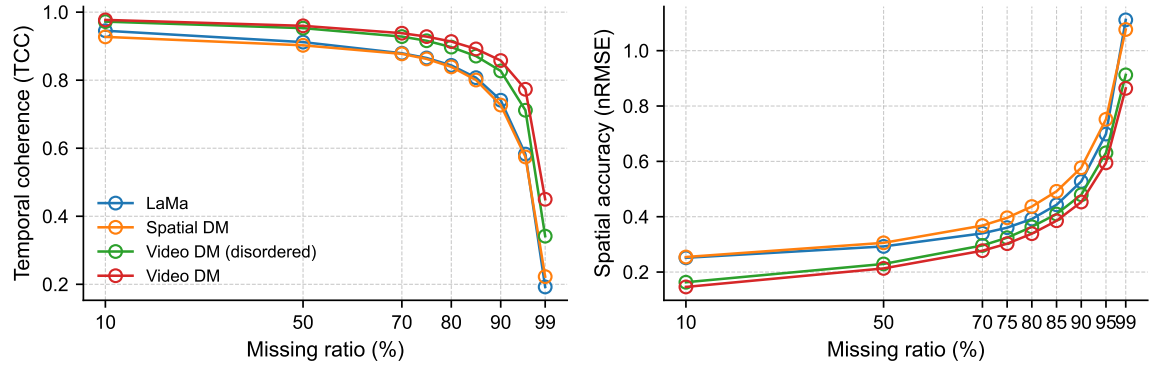


Fig. S5 Sensitivity analysis of temporal information integration. Quantitative comparison of reconstruction performance (Mean TCC, left; Mean nRMSE, right) on synthetic ERA5 temperature data at 5° spatial resolution across varying sparsity levels. To isolate the contribution of temporal context, our Video DM (red) is compared against three architectural baselines: LaMa (blue, spatial-only), normal spatial DM (orange, snapshot-based diffusion), and Video DM (disordered) (green). For the disordered variant, the model was trained on temporally randomized sequences to disrupt dynamic continuity but evaluated on ordered sequences identical to our Video DM. All DM metrics (orange, green, red) represent the ensemble mean of 50 generated members. The performance gap between our Video DM and the disordered baseline confirms that the model's accuracy stems from learning genuine temporal dynamics during training, rather than merely exploiting spatial correlations.

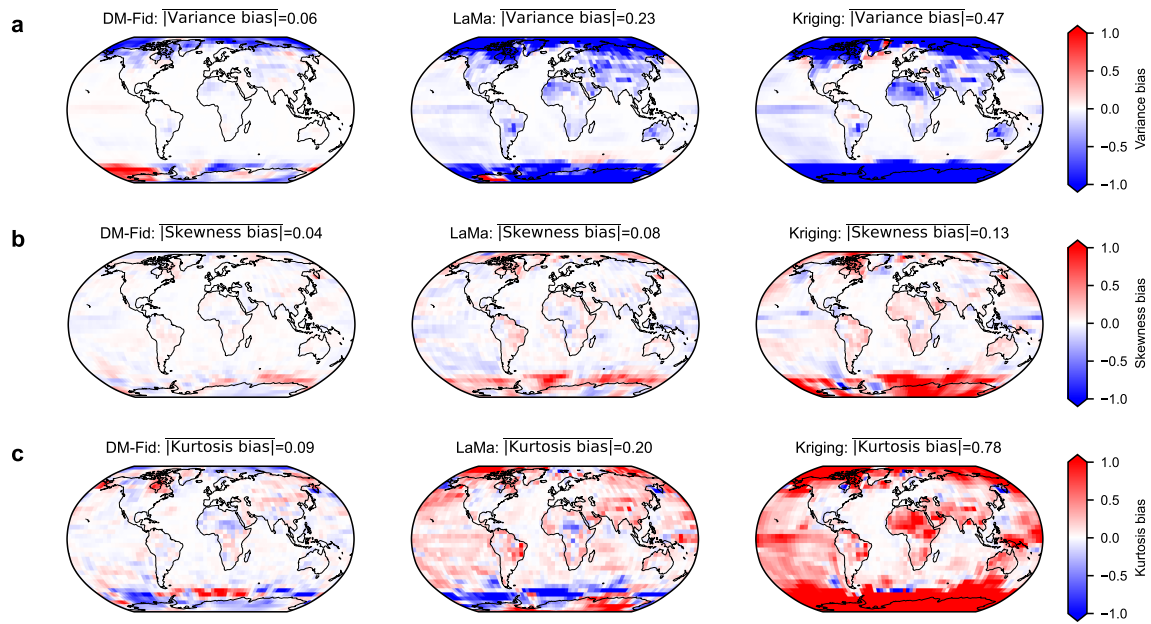


Fig. S6 Preservation of higher-order statistics of climate dynamics. Global maps of bias in key statistical moments derived from the CMIP6 heldout member (1850–2014) using HadCRUT5 coverage. **a**, Variance bias; **b**, Skewness bias; and **c**, Kurtosis bias. The DM-Fid reconstruction (left column) maintains low bias across all higher-order indicators, confirming it captures the amplitude and character of temperature variability. In contrast, LaMa and Kriging exhibit severe variance collapse (indicated by high positive bias maps where variance is underestimated) and fail to reproduce the tail statistics (skewness/kurtosis) essential for extreme event analysis.

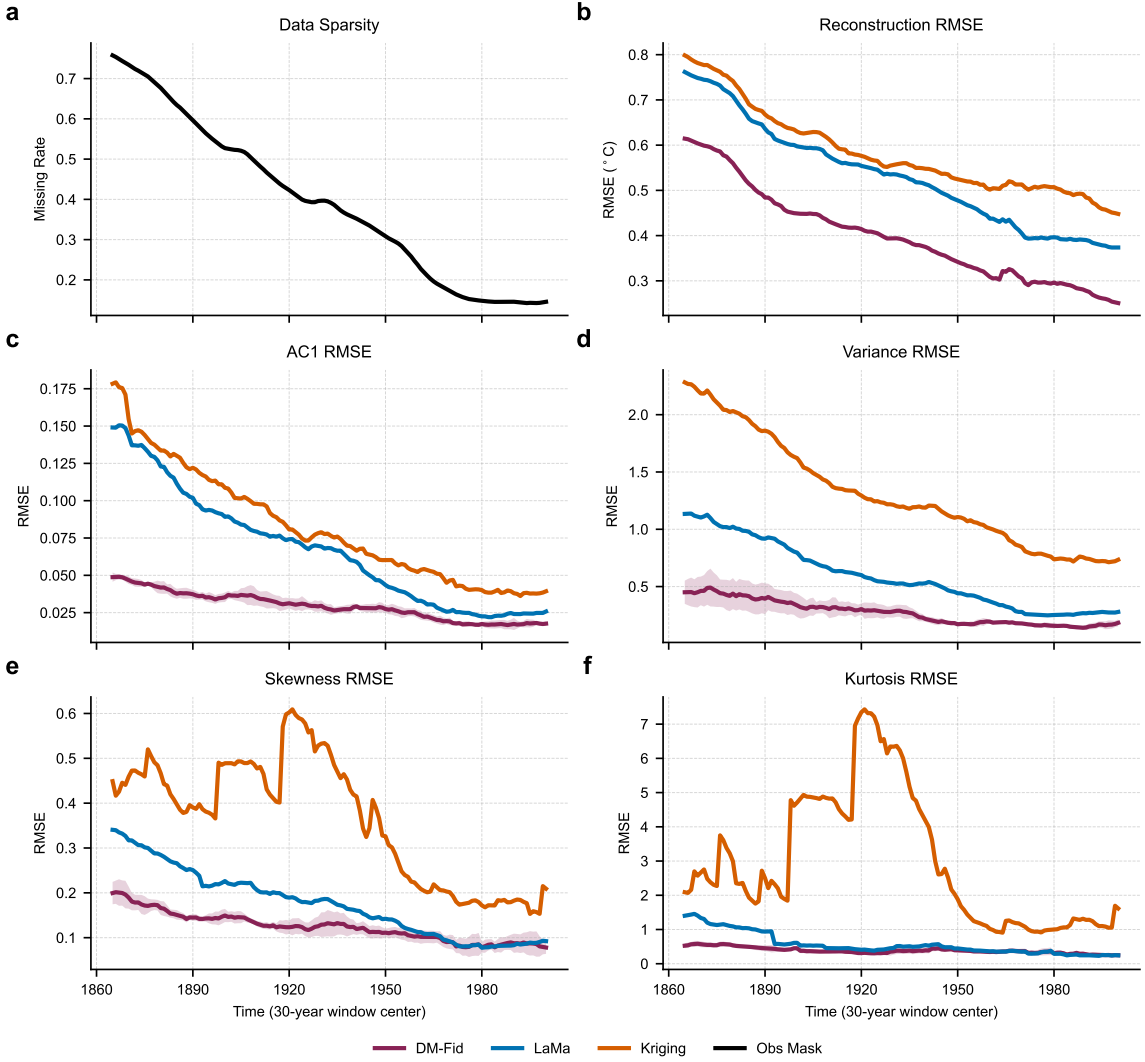


Fig. S7 Reconstruction accuracy and statistical stability under varying observational coverage. **a**, Time series of the spatially weighted missing rate (data sparsity) derived from the HadCRUT5 observational mask. **b**, Reconstruction RMSE calculated specifically over unobserved regions, comparing the DM-Fid mean against LaMa and Kriging. **c–f**, Temporal evolution of the RMSE for higher-order statistical properties: **c**, Lag-1 autocorrelation (AC1); **d**, Variance; **e**, Skewness; and **f**, Kurtosis. Metrics are computed using a 30-year sliding window (1850–2014) on the CMIP6 held-out member. Shaded regions for DM-Fid indicate the ensemble spread (mean \pm 1.96 std. dev.) across 5 generated members. While Kriging (orange) and LaMa (blue) exhibit error trajectories that strongly correlate with historical data sparsity, showing significant degradation during the data-poor early 20th century, DM-Fid (purple) maintains a consistently low and stable error profile throughout the entire timeline, demonstrating robust preservation of statistical characteristics even under severe observational sparsity.

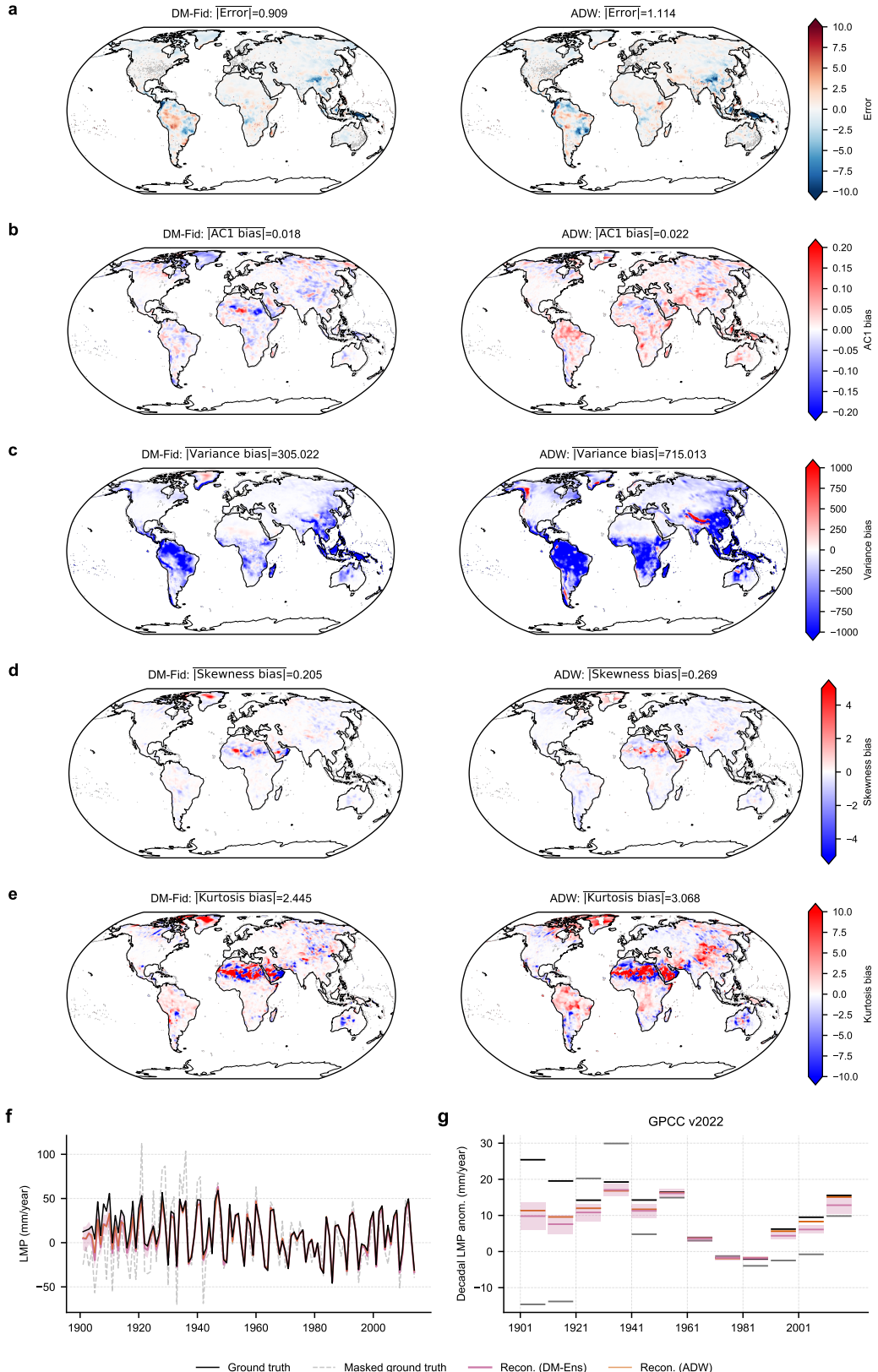


Fig. S8 Evaluation of historical precipitation dynamics. Evaluation of precipitation reconstruction (0.5°) using the sparse GPCC v2022 observational mask applied to the CMIP6 heldout member (1901–2014). **a**, Mean absolute error map. **b–e**, Bias maps for dynamical indicators: **b**, AC1; **c**, Variance; **d**, Skewness; **e**, Kurtosis. Note the massive variance bias in the ADW method (**c**, right), caused by its reversion to climatology in data-void regions. **f**, Monthly global land mean precipitation (LMP) residuals. **g**, Decadal LMP anomalies. The pink ranges represent the spread of the DM-Ens ($N=50$), with the ground truth (black lines) mostly falling within the model's uncertainty range.

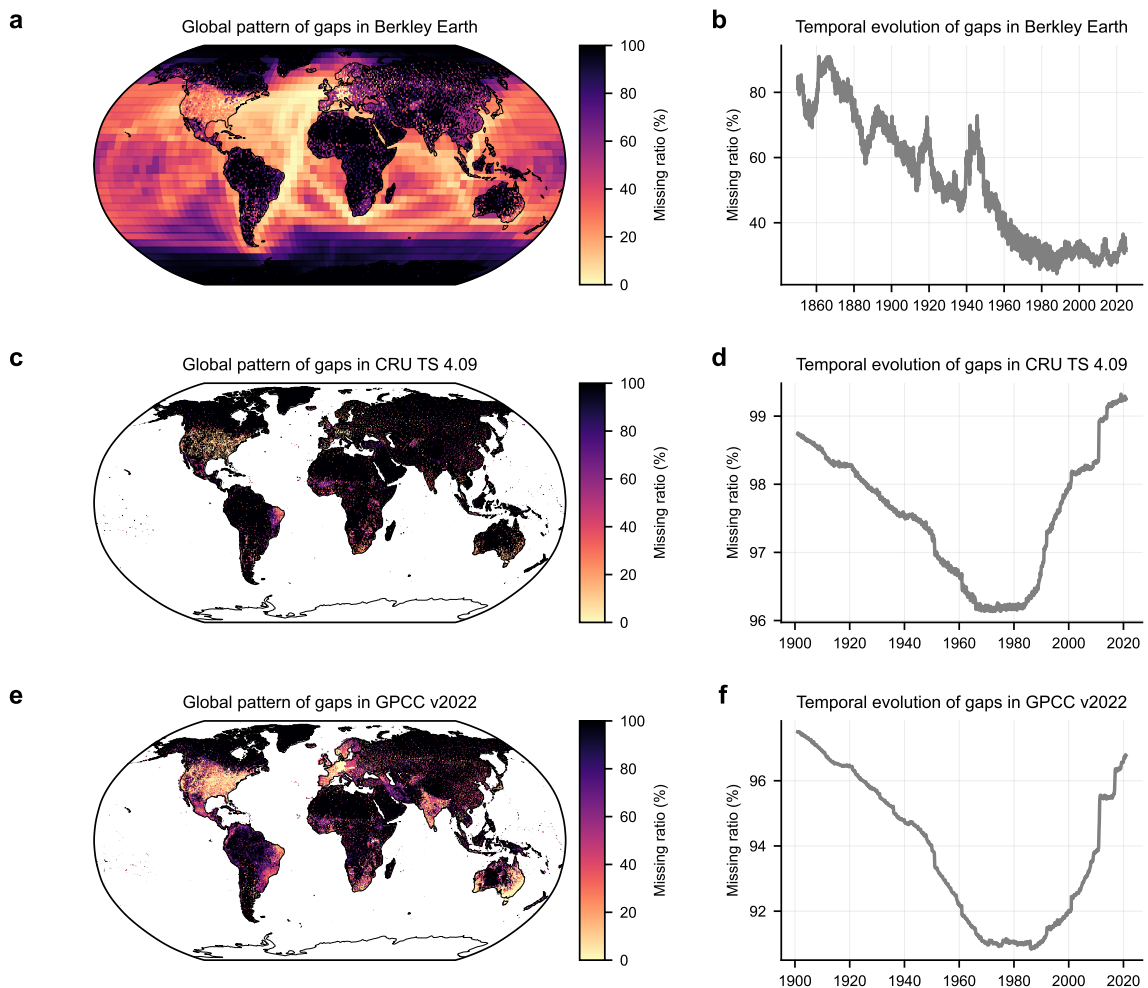


Fig. S9 Spatiotemporal evolution of observational coverage. **a, c, e**, Global maps showing the percentage of missing data per grid cell over the historical period for the three key observational datasets used to generate masks: **a**, Berkley Earth (Temperature; 1850–2024); **c**, CRU TS 4.09 (Precipitation; 1901–2020); **e**, GPCC v2022 (Precipitation; 1901–2020). **b, d, f**, Time series of the global missing data ratio for each respective dataset.

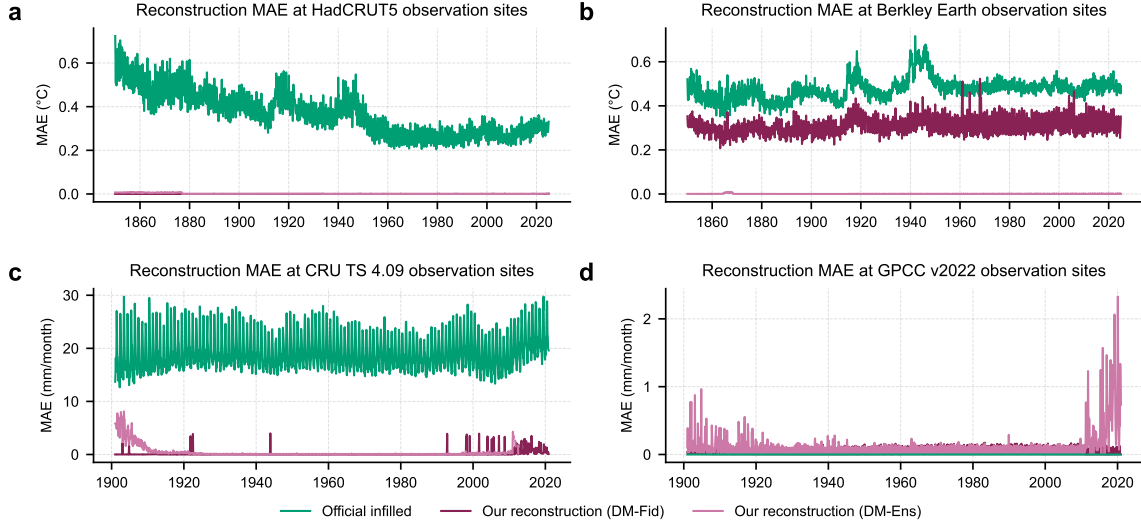


Fig. S10 Reconstruction error at observational sites. Time series of the spatial Mean Absolute Error (MAE) calculated exclusively at grid cells containing observational data. **a**, HadCRUT5 temperature. **b**, Berkeley Earth temperature. Note that the DM-Fid reconstruction in **b** exhibits a non-zero but consistently lower error than the official product; this is because it performs a challenging simultaneous downscaling (using 5° sea-surface inputs) and gap-filling task, rather than simple interpolation. **c**, CRU TS 4.09 precipitation. **d**, GPCC v2022 precipitation. In **d**, the official product shows near-zero error because the raw station data are not publicly available, forcing the use of the infilled product itself as the reference at station locations. However, the DM-Ens error magnitude remains negligible (< 2 mm/month) compared to the typical interpolation errors seen in CRU TS (panel **c**), confirming our model's robustness.

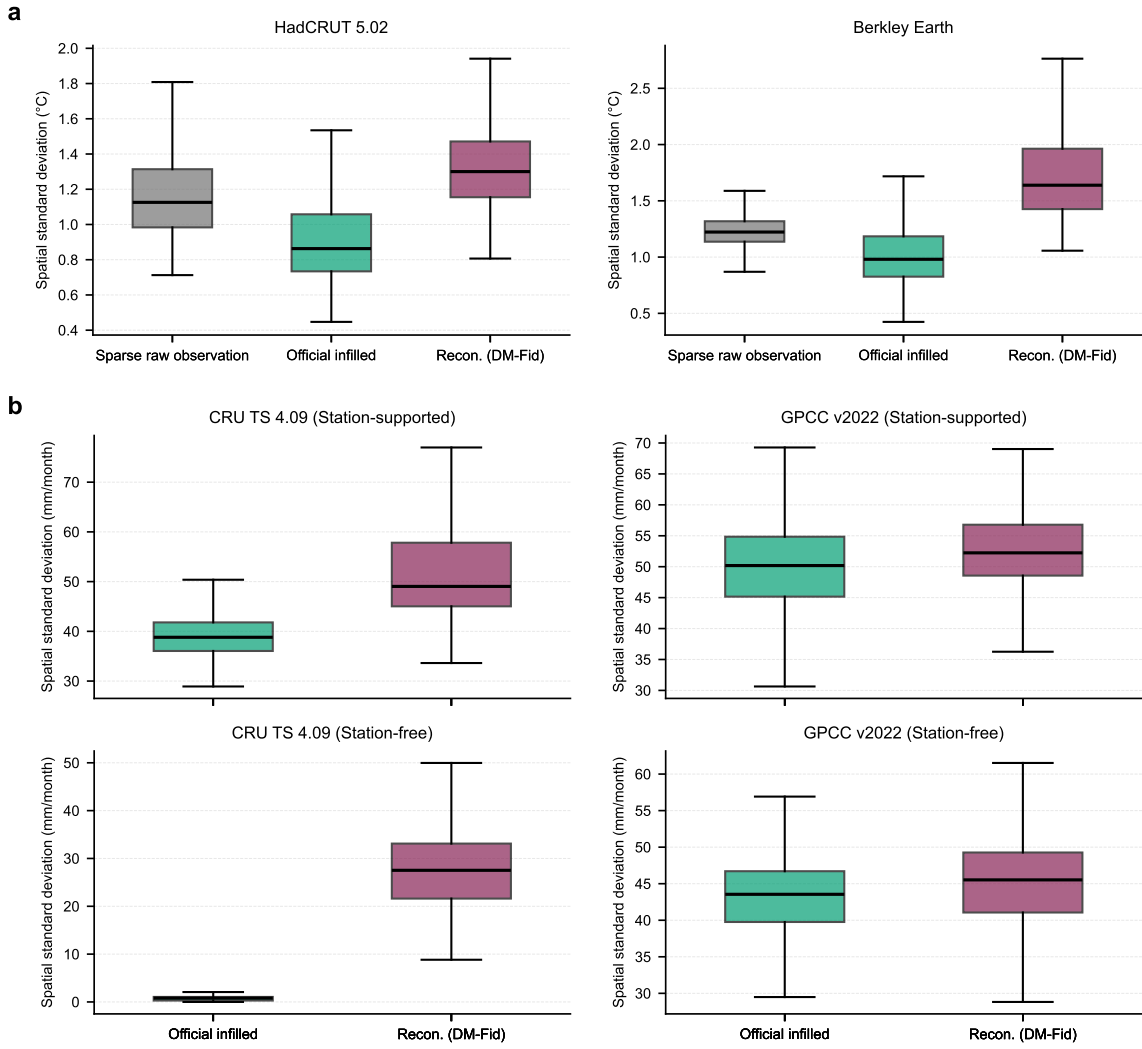


Fig. S11 Quantification of the variance deficit in official infilled products. Boxplots summarizing the distribution of monthly spatial standard deviations calculated across the full historical period. **a**, Temperature anomalies (HadCRUT5, Berkeley Earth). Official infilled products (green) exhibit consistently lower spatial variance compared to the sparse raw observations (grey), indicating a loss of signal amplitude due to smoothing. The DM-Fid reconstruction (purple) restores variance to levels consistent with or slightly exceeding the raw inputs. **b**, Precipitation anomalies (CRU TS 4.09, GPCC v2022), stratified by grid cells with (Station-supported) and without (Station-free) direct observations. The variance deficit is most acute in station-free regions: CRU TS collapses to near-zero variance (climatology), and GPCC also shows suppressed variability. In contrast, DM-Fid maintains more realistic spatial heterogeneity in unobserved regions.

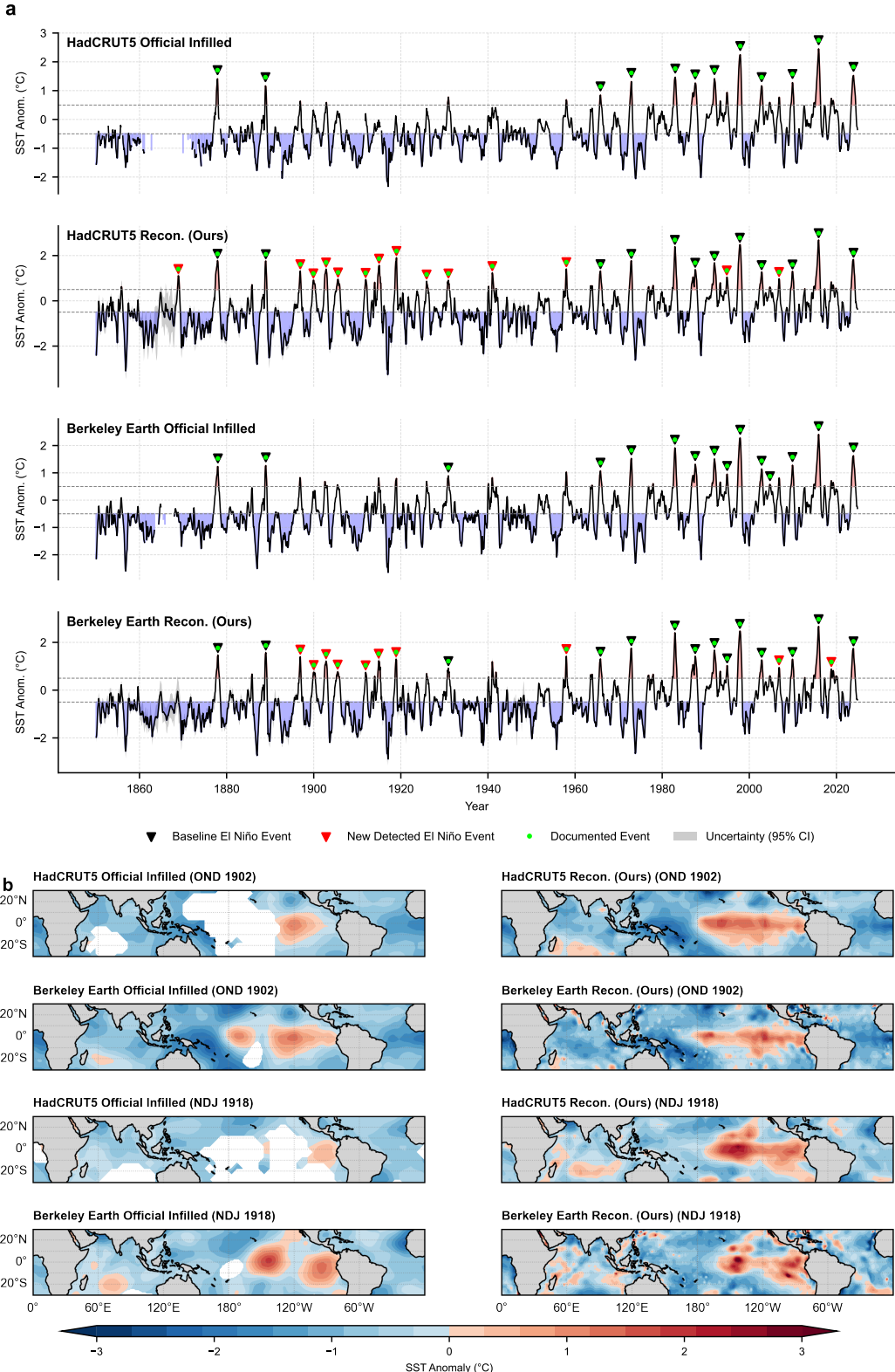


Fig. S12 Investigation of historical El Niño-Southern Oscillation (ENSO) variability. **a**, Time series comparison of Niño 3.4 Sea Surface Temperature (SST) anomalies derived from official infilled products (HadCRUT5, top; Berkeley Earth, bottom) versus our generative reconstruction. Black triangles denote El Niño events detected in the official infilled products, defined by a 3-month running mean of Niño 3.4 SST anomalies exceeding the anomaly threshold for at least 5 consecutive months. Red triangles in the reconstruction panels indicate newly detected events using the same criteria in our generative reconstruction. Green dots superimposed on the triangles identify events that are explicitly documented in historical literature and NOAA records [54–56]. Grey shading represents continuous uncertainty quantification (1.96σ). **b**, Spatial snapshots of SST anomalies during two early 20th-century El Niño events: Late 1902 (OND) and the 1918–1919 event (NDJ). Comparisons between the official infilled baselines (left column) and our generative reconstruction (right column) highlight the model’s ability to resolve the canonical ‘bull’s tongue’ spatial pattern of equatorial warming, which appears diffuse or muted in the infilled products during these data-sparse periods.

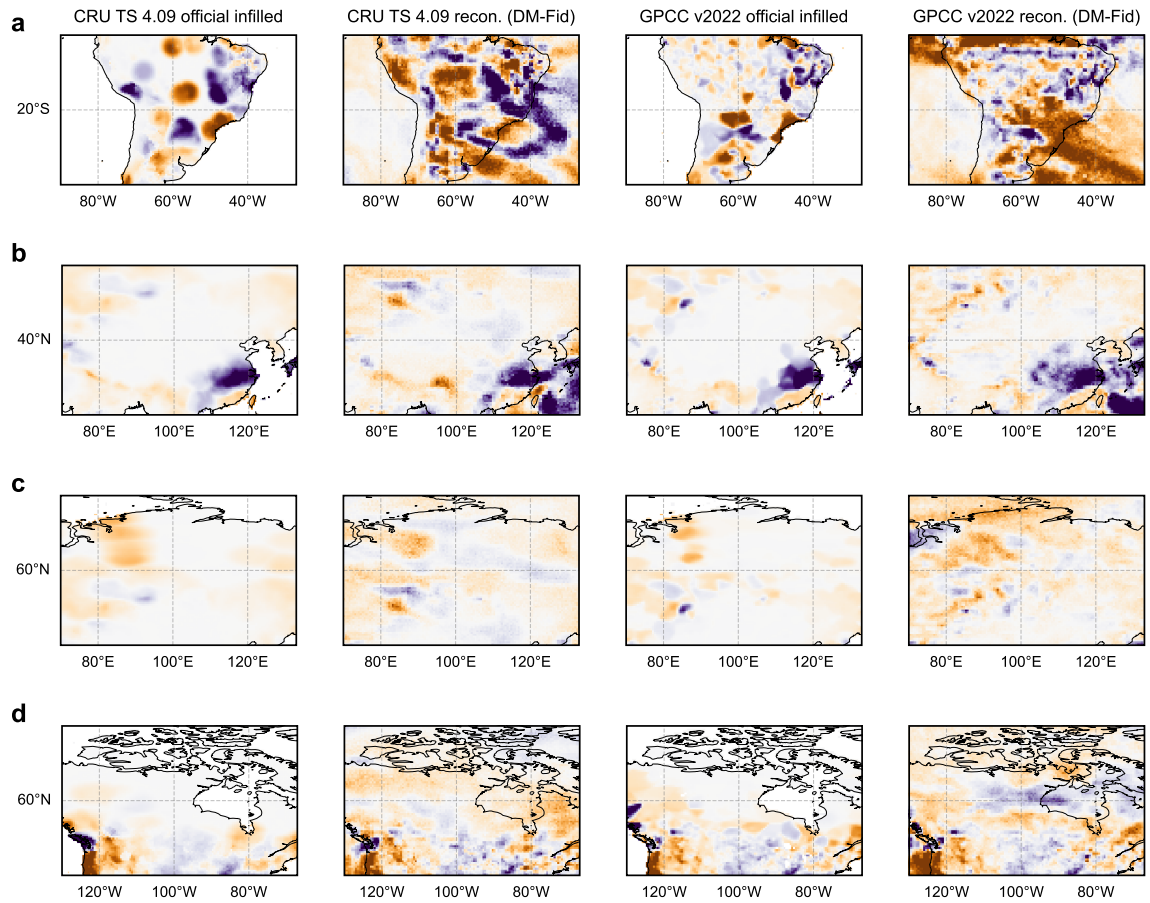


Fig. S13 Regional comparison of precipitation reconstruction versus official infilled products in data-sparse regions. **a-d**, Snapshots of precipitation anomalies in December 1918 over **a**, South America, **b**, China, **c**, Siberia, and **d**, Canada. Columns display the official infilled baselines and our DM-Fid reconstructions for the CRU TS 4.09 and GPCC v2022 datasets, respectively. Note that while the official products exhibit broad, smoothed patterns due to the sparsity of observations in these regions, our reconstructions recover distinct, high-amplitude local heterogeneity. The color scale corresponds to that in Fig. 5b.

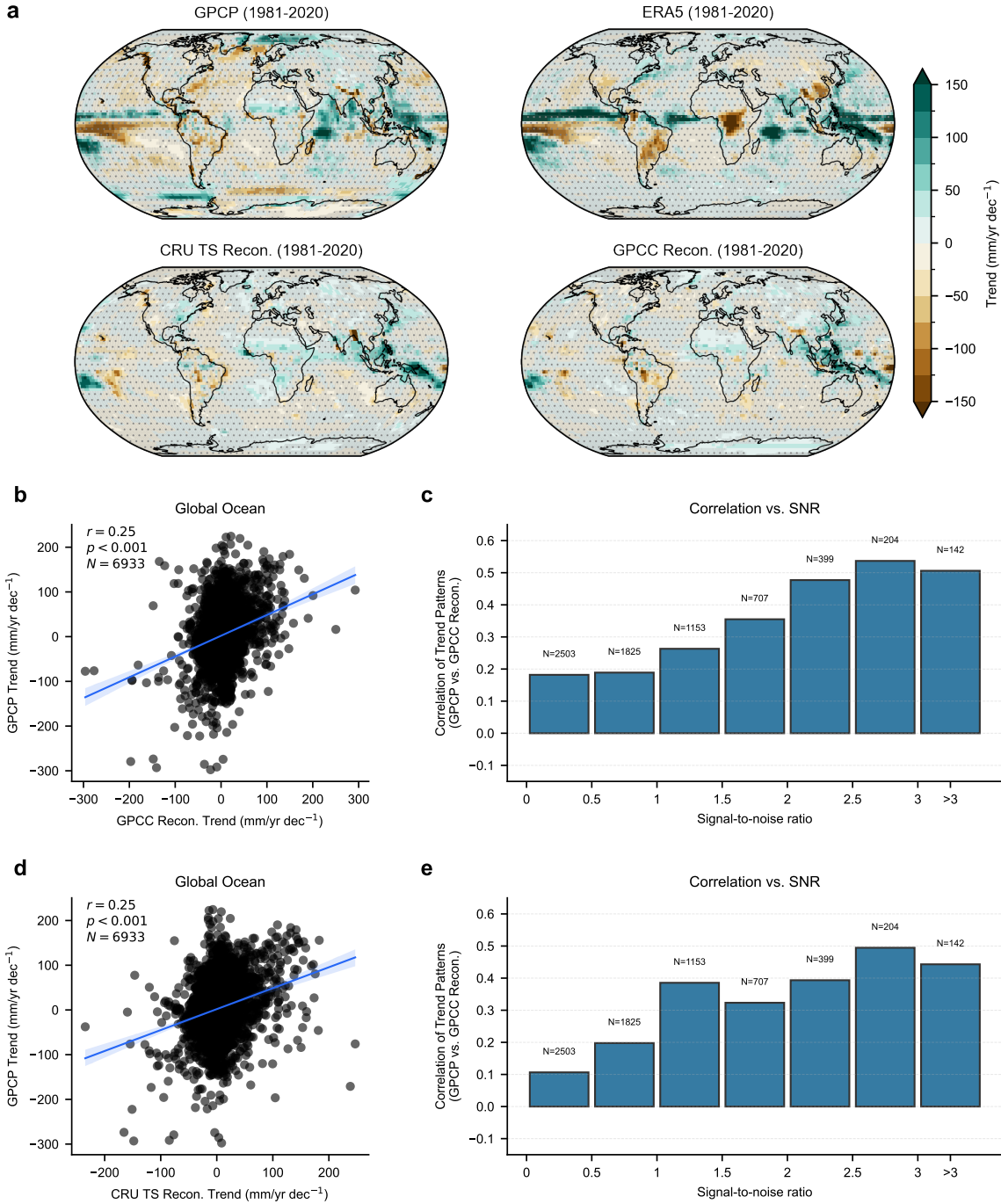


Fig. S14 Evaluation of reconstructed precipitation trends across land and ocean (1981–2020). **a**, Global maps of linear precipitation trends comparing the satellite-gauge merged GPCP product (top left) and ERA5 reanalysis (top right) against our reconstructions conditioned on land-only inputs from CRU TS (bottom left) and GPCC (bottom right). Regions with statistically non-significant trends ($p \geq 0.05$) are masked with gray shading and stippling. Statistical significance is assessed to control for serial correlation and multiple testing: for GPCP and ERA5, significance is determined via an AR(1) adjustment [61] followed by a False Discovery Rate (FDR) procedure [62]; for the reconstructions, AR(1)-adjusted p -values from individual ensemble members are first aggregated using Fisher's method, followed by an FDR correction. **b–e**, Quantitative evaluation of oceanic precipitation trends. Scatter plots (**b**, **d**) compare oceanic trends from GPCP observations against reconstructions derived from GPCC (**b**) and CRU TS (**d**) over the Global Ocean. Histograms (**c**, **e**) show the correlation as a function of the signal-to-noise ratio (SNR) in the GPCP data. Notably, the trend correlation between GPCP and ERA5 (which directly assimilates satellite data) is limited to $r = 0.49$ over the global ocean, establishing an effective observational ceiling for reconstruction accuracy. In this context, our reconstruction ($r = 0.25$), inferred exclusively from terrestrial constraints via learned teleconnections, recovers a substantial fraction of the oceanic trend signal given the inherent uncertainties in observational records.

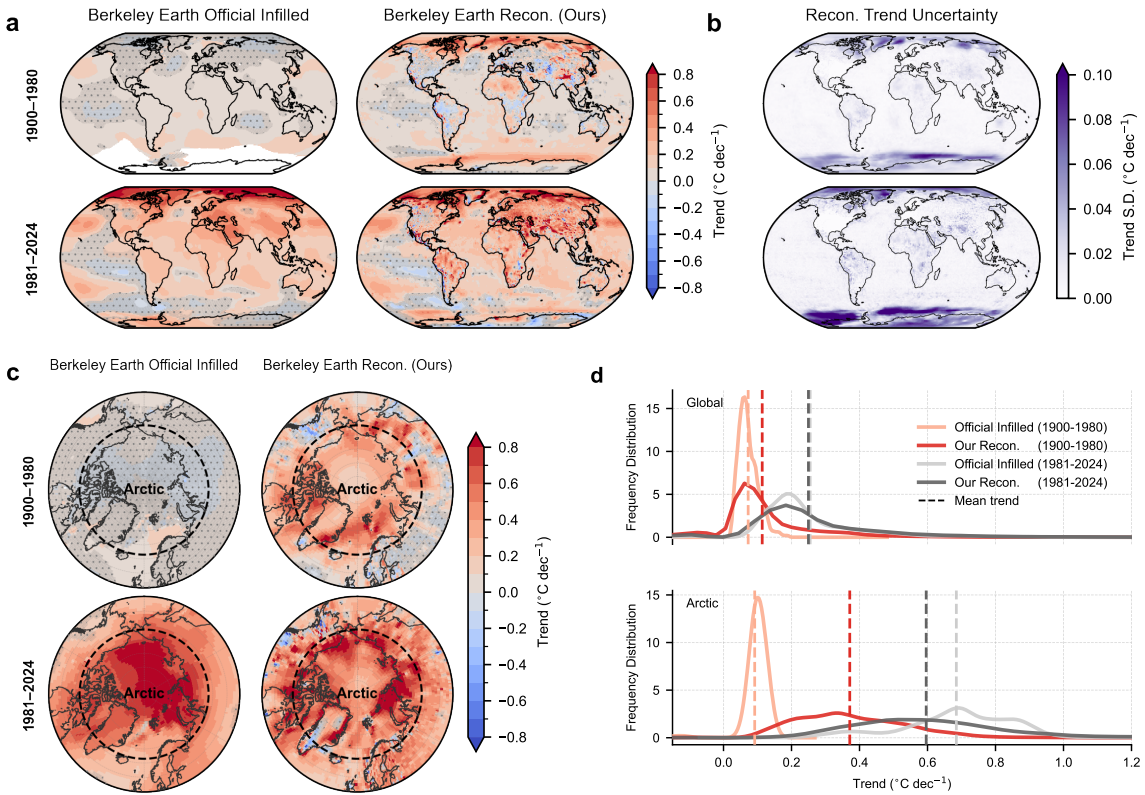


Fig. S15 Re-evaluating historical temperature trends using the Berkeley Earth. **a**, Global linear temperature trends ($^{\circ}\text{C dec}^{-1}$) for the official infilled Berkeley Earth and our DM-Fid reconstruction (ensemble mean) across pre-satellite (1900–1980) and satellite (1981–2024) eras. Regions with statistically non-significant trends ($p \geq 0.05$) are masked with gray shading and stippling. Statistical significance is assessed following an AR(1) adjustment after ref.[61] to account for serial correlation. For the official infilled product, the resulting p -values are subsequently adjusted using a False Discovery Rate (FDR) control [62]. For our reconstruction, the AR(1)-adjusted p -values from the ensemble members are combined using Fisher's method, followed by an FDR correction to strictly control for false discoveries. **b**, Uncertainty of the reconstructed trends, quantified as the standard deviation of the trend maps derived from the individual DM-Fid ensemble members. **c**, Localized temperature trends shown in **a**, highlighting the Arctic region (dashed). **d**, Frequency distribution of area-weighted statistically significant temperature trends, estimated via Gaussian kernel density estimation (KDE). Vertical dashed lines indicate the mean trend (area-weighted averaging from statistically significant trends) for each distribution.

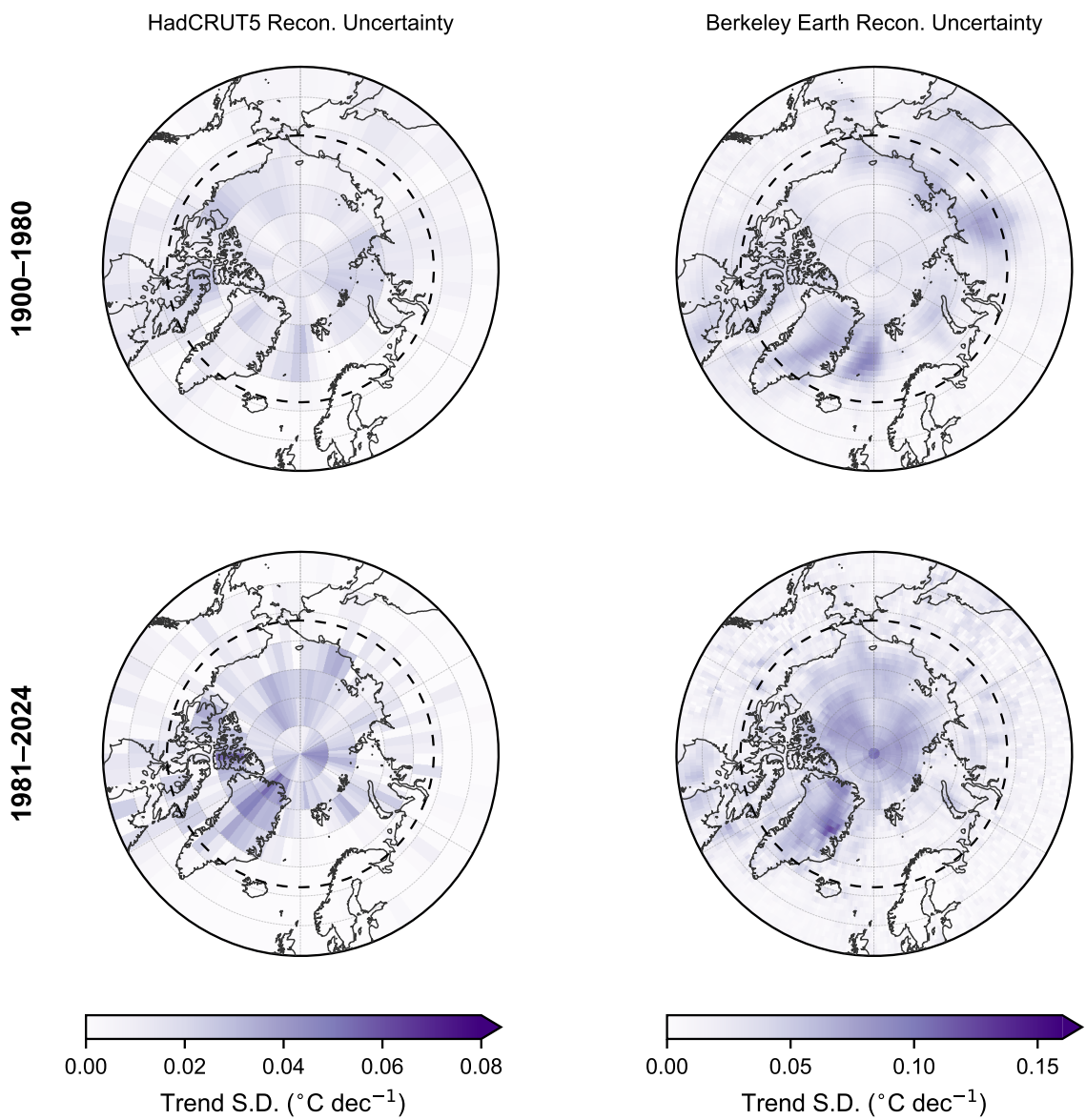


Fig. S16 Localized uncertainty of reconstructed Arctic trends. Spatial maps of trend uncertainty, quantified as the standard deviation of the five trend maps derived from the individual DM-Fid ensemble members. Columns display results for the HadCRUT5 (left) and Berkeley Earth (right) reconstructions. Rows correspond to the pre-satellite (1900–1980, top) and satellite (1981–2024, bottom) eras. These fields provide the uncertainty context for the Arctic warming patterns analyzed in Fig. 6 and Supplementary Fig. S15, identifying regions of lower confidence (darker purple) where the ensemble members diverge.

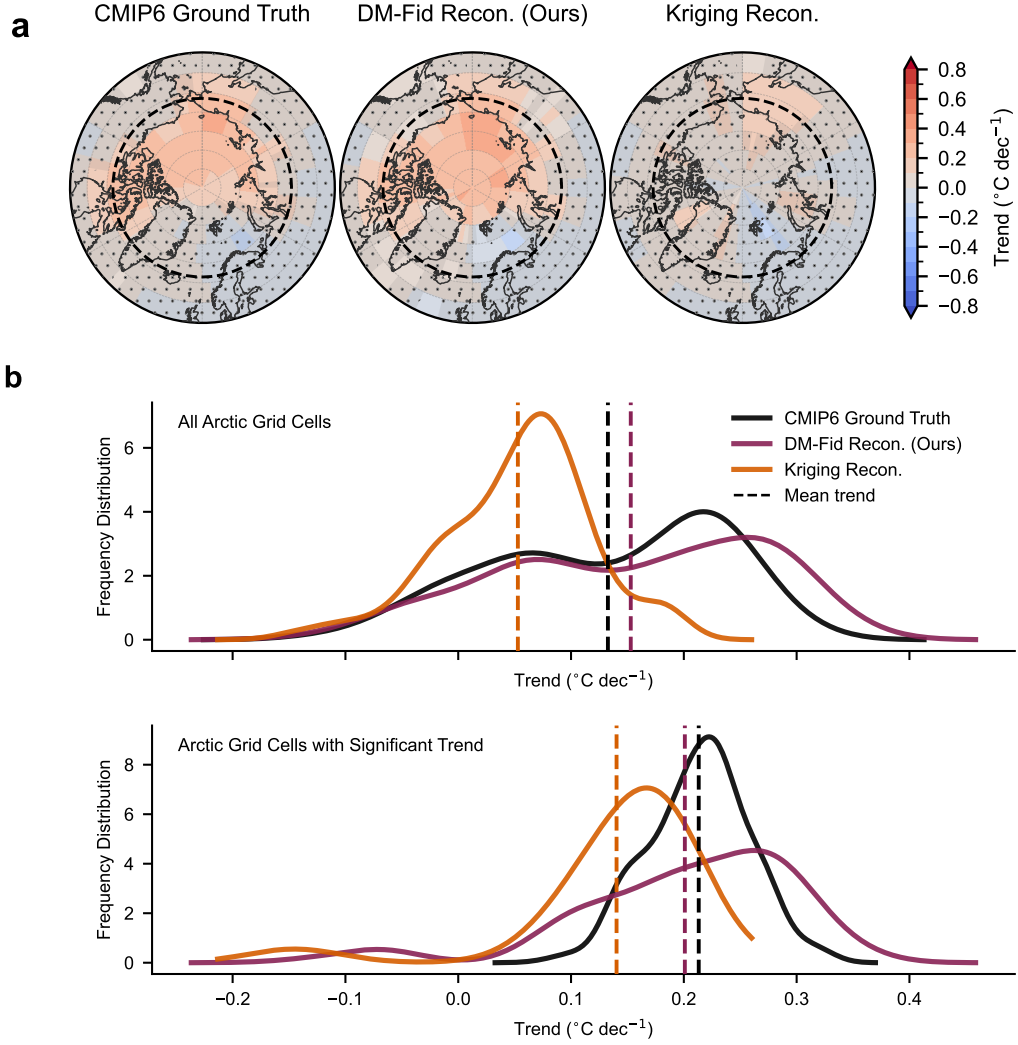


Fig. S17 Evaluation of trend reconstruction biases using a controlled CMIP6 experiment. To elucidate the structural discrepancies between our reconstruction and official products in data-sparse regions, we performed a controlled experiment using the hold-out CMIP6 historical simulations at 5° spatial resolution. **a**, Comparison of linear temperature trends ($^{\circ}\text{C dec}^{-1}$) in the Arctic region derived from: the complete CMIP6 simulation ground truth (left); our DM-Fid reconstruction (center); and Kriging interpolation (right). Reconstructions are generated using sparse synthetic observations sampled according to the realistic historical coverage mask of HadCRUT5. Regions with statistically non-significant trends ($p \geq 0.05$) are masked with gray stippling. Statistical significance is assessed following an AR(1) adjustment[61] to account for serial correlation. For the DM-Fid reconstruction, p -values from ensemble members are combined using Fisher's method followed by False Discovery Rate (FDR) control; for the CMIP6 Ground Truth and Kriging interpolation, a standard FDR procedure is applied. **b**, Frequency distribution of area-weighted trends in the Arctic estimated via Gaussian kernel density estimation. The top panel includes all grid cells, while the bottom panel is restricted to statistically significant trends. Vertical dashed lines indicate the mean trend for each method. Crucially, Kriging interpolation (orange) results in a distinct negative shift of the distribution, leading to a systematic underestimation of the mean warming rate relative to the ground truth (black). In contrast, the DM-Fid reconstruction (purple) accurately recovers the distribution profile and central tendency of the CMIP6 ground truth. This validates that the higher historical warming rates recovered by our method (as seen in Fig. 6d) are likely a correction of the smoothing bias inherent to conventional interpolation.

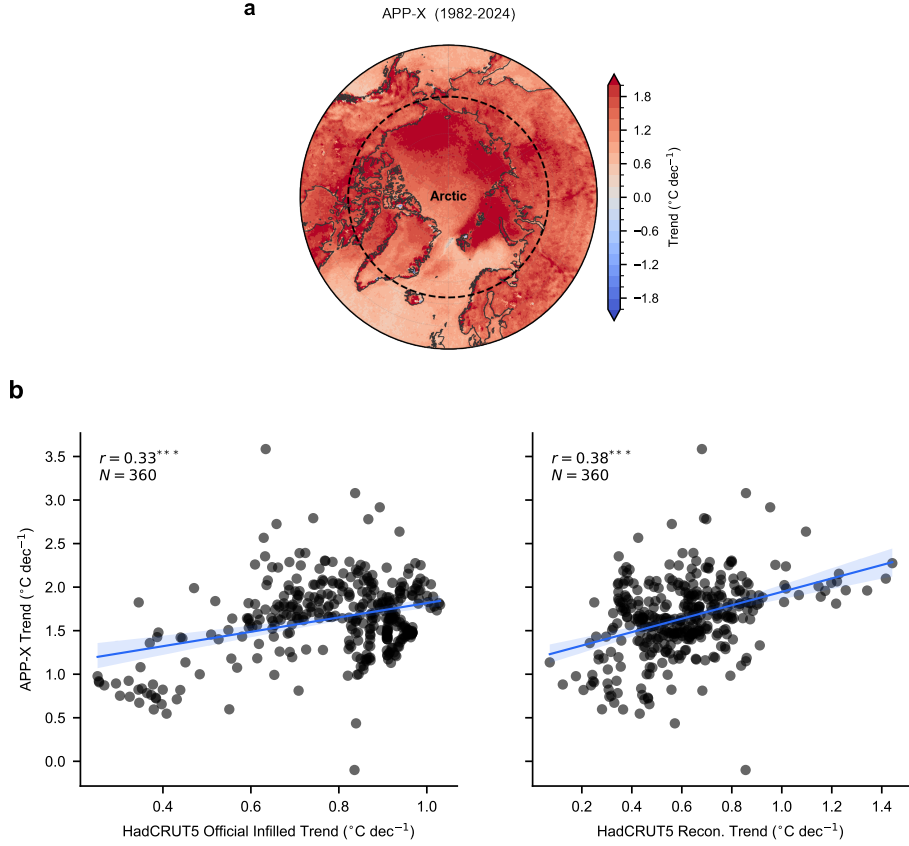


Fig. S18 Validation of modern Arctic warming patterns against independent satellite data. **a**, Spatial map of linear surface temperature trends over the Arctic derived from the independent AVHRR Polar Pathfinder (APP-X) dataset during the satellite era. Regions with statistically non-significant trends ($p \geq 0.05$) are masked with gray stippling. Statistical significance is assessed following an AR(1) adjustment[61] to account for serial correlation, followed by a False Discovery Rate (FDR) control. **b**, Spatial correlation analysis comparing the trend patterns in the Arctic of independent APP-X satellite observations against the official HadCRUT5 infilled product (left) and our DM-Fid reconstruction (right). Each point corresponds to a grid cell in the Arctic region (Lat $> 66.5^{\circ}\text{N}$).

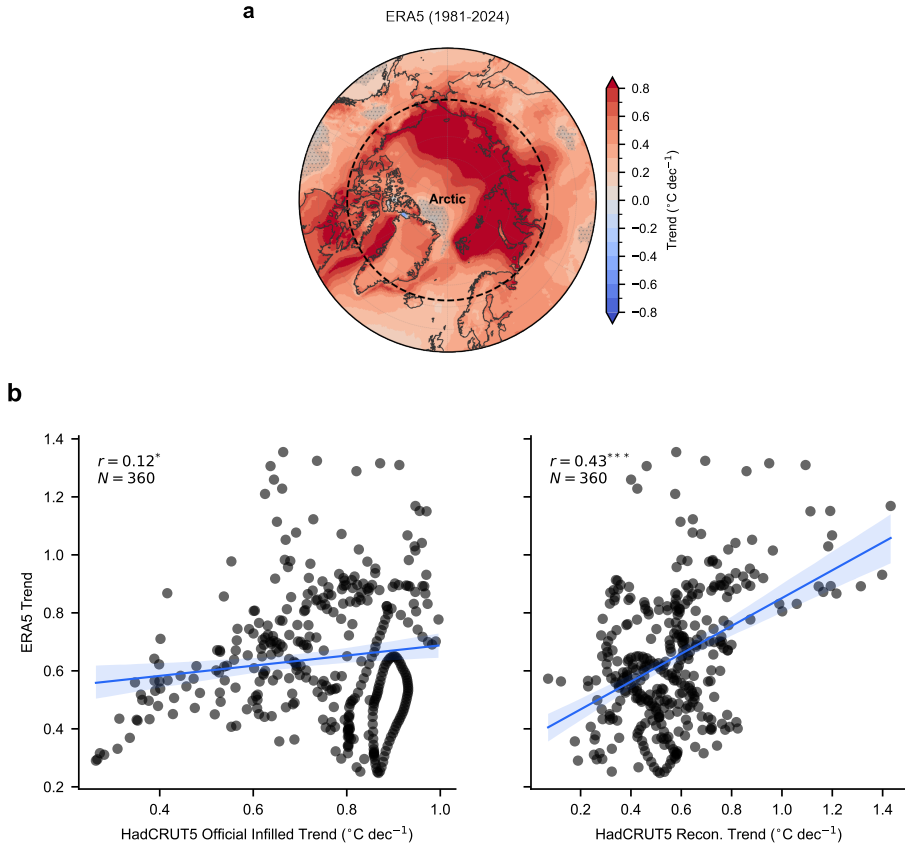


Fig. S19 Validation of modern Arctic warming patterns against independent ERA5 reanalysis data. **a**, Spatial map of linear surface temperature trends over the Arctic derived from the independent ERA5 reanalysis during the satellite era. Regions with statistically non-significant trends ($p \geq 0.05$) are masked with gray stippling. Statistical significance is assessed following an AR(1) adjustment[61] to account for serial correlation, followed by a False Discovery Rate (FDR) control. **b**, Spatial correlation analysis comparing the trend patterns in the Arctic of reanalysis against the HadCRUT5 official infilled product (left) and our DM-Fid reconstruction (right). Each point corresponds to a grid cell in the Arctic region (Lat $> 66.5^{\circ}\text{N}$).

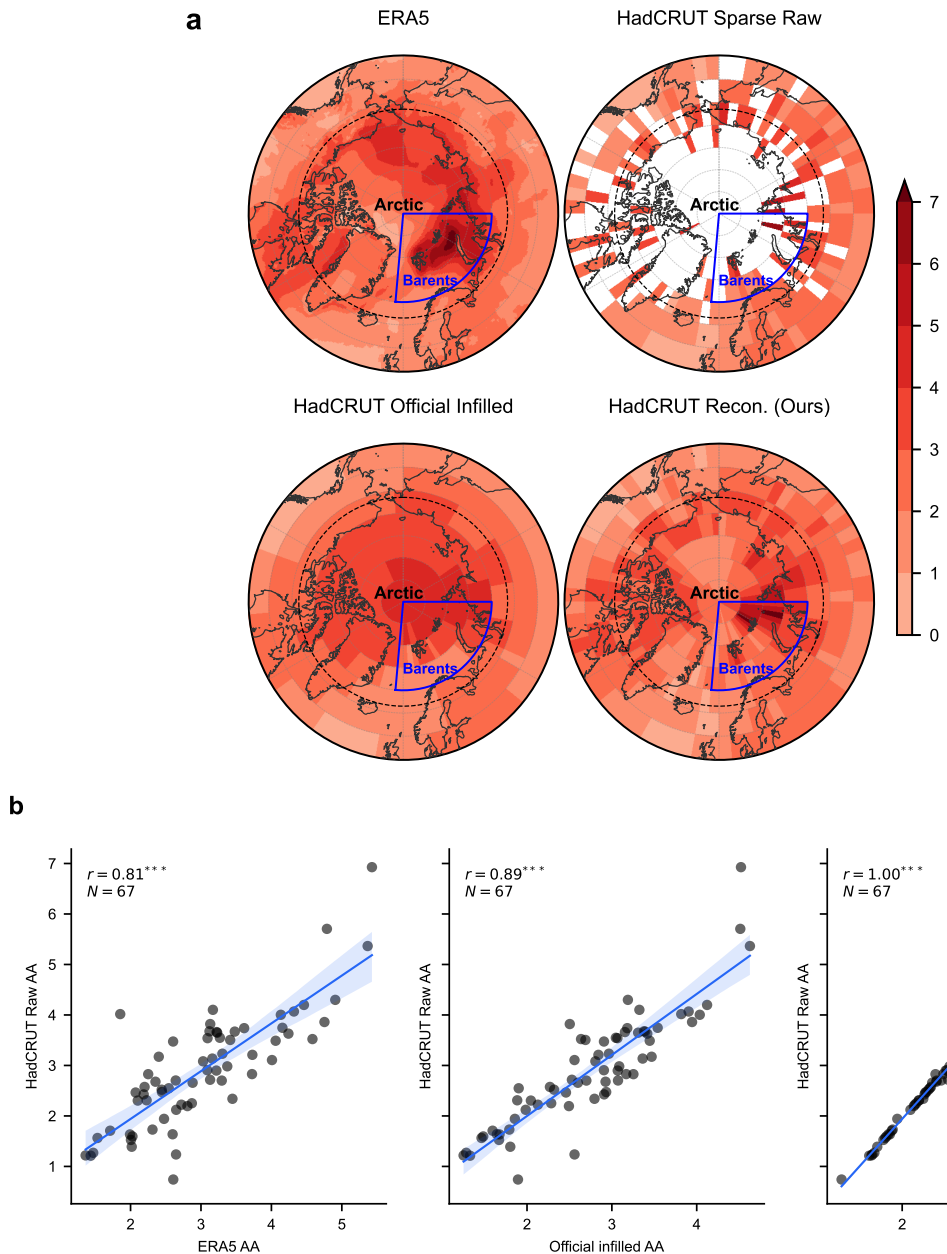


Fig. S20 Validation of local Arctic amplification against sparse in-situ observations. **a**, Spatial maps of the local warming amplification factor (defined as the ratio of the local linear trend to the global mean trend) over the Arctic region (Lat $> 66.5^{\circ}\text{N}$). Comparison includes the ERA5 reanalysis (top left), the raw sparse HadCRUT5 observations (top right), the official infilled HadCRUT5 product (bottom left), and our DM-Fid reconstruction (bottom right). **b**, Scatter plots quantifying the consistency of local amplification factors derived from the three complete datasets (*x*-axis) against the raw sparse observational ground truth (*y*-axis). Each point represents a grid cell within the Arctic region where in situ observational data is available.

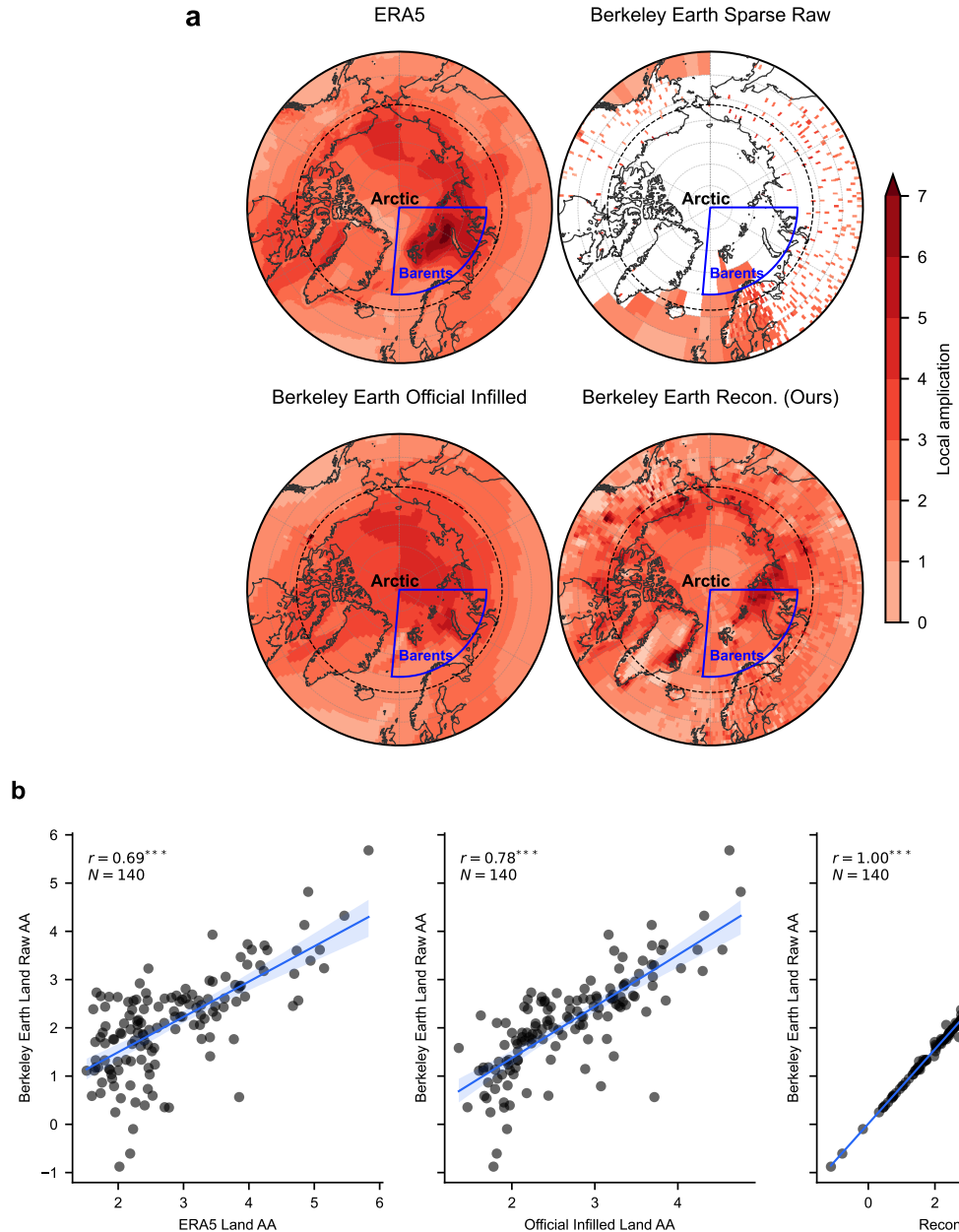


Fig. S21 Validation of local Arctic amplification fidelity against sparse in-situ land observations (Berkeley Earth). **a**, Spatial maps of the local warming amplification factor over the Arctic region (Lat > 66.5°N). Comparison includes the ERA5 reanalysis (top left), the raw sparse Berkeley Earth observations (top right), the official Berkeley Earth infilled product (bottom left), and our DM-Fid reconstruction (bottom right). Note that the raw observational baseline (top right) is limited to land stations, as Berkeley Earth interpolates ocean temperatures from external sea surface temperature datasets. **b**, Scatter plots quantifying the consistency of local amplification factors derived from the three complete datasets (*x*-axis) against the raw sparse land observational ground truth (*y*-axis). The analysis is restricted to grid cells containing land stations.

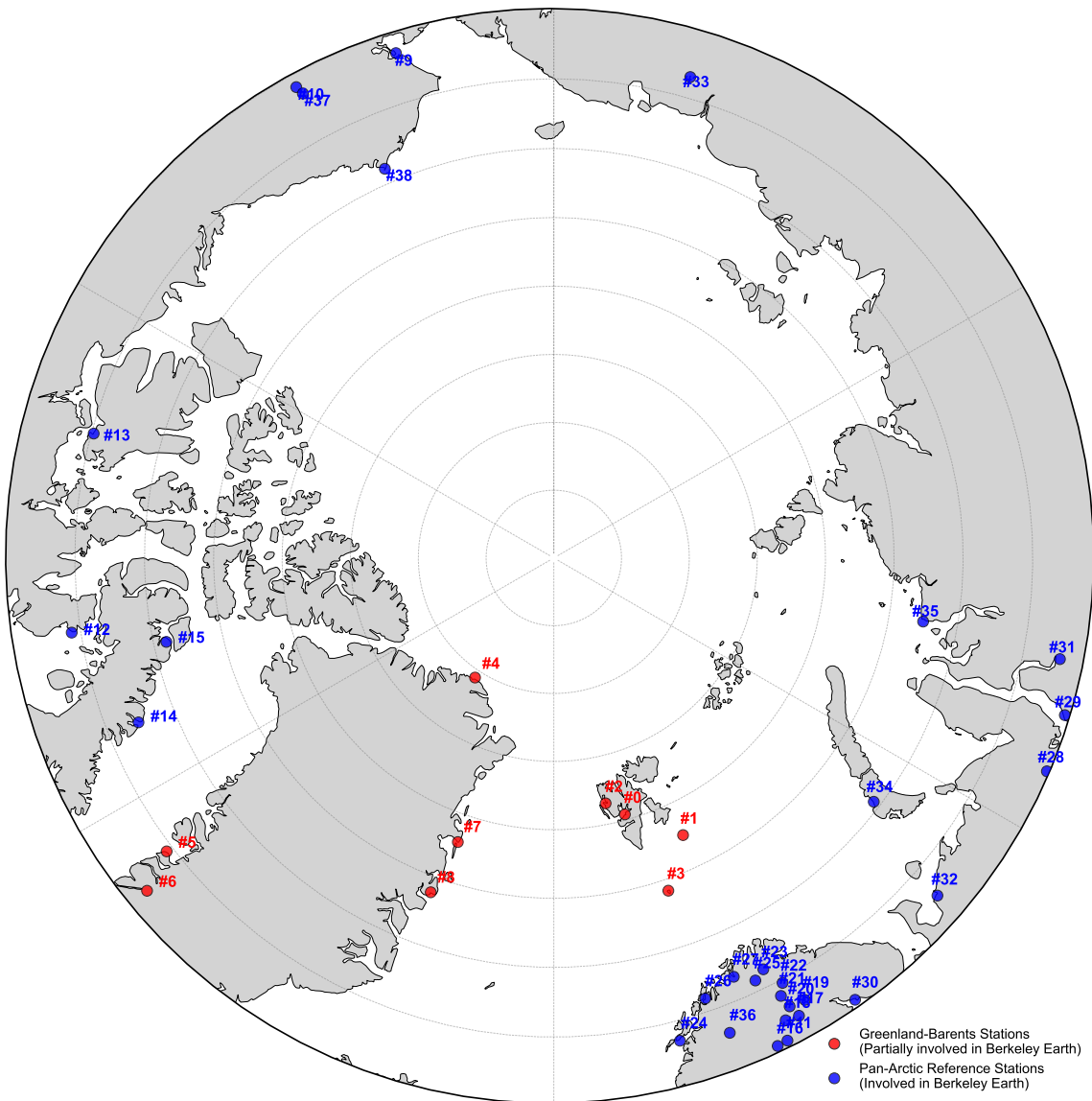


Fig. S22 Location map of Arctic weather stations (1981–2024). The map displays the positions of 39 ground-based weather stations with seamless observational records used to validate local warming trends ($\text{Lat} > 66.5^\circ\text{N}$). Stations are classified into two groups. (i) Greenland-Barents stations (red markers): Stations primarily located in high-sensitivity warming zones (Barents Sea and Greenland). These are labeled ‘partially involved’ because their records within the Berkeley Earth dataset are highly fragmented or discontinuous during the 1981–2024 period, but have been supplemented here to ensure seamless coverage for validation. These provide critical validation for intense warming signals. (ii) Pan-Arctic reference stations (blue markers): Stations distributed across the wider Arctic that are fully involved in the standard Berkeley Earth archive. Station IDs correspond to the performance metrics in Supplementary Table S3.

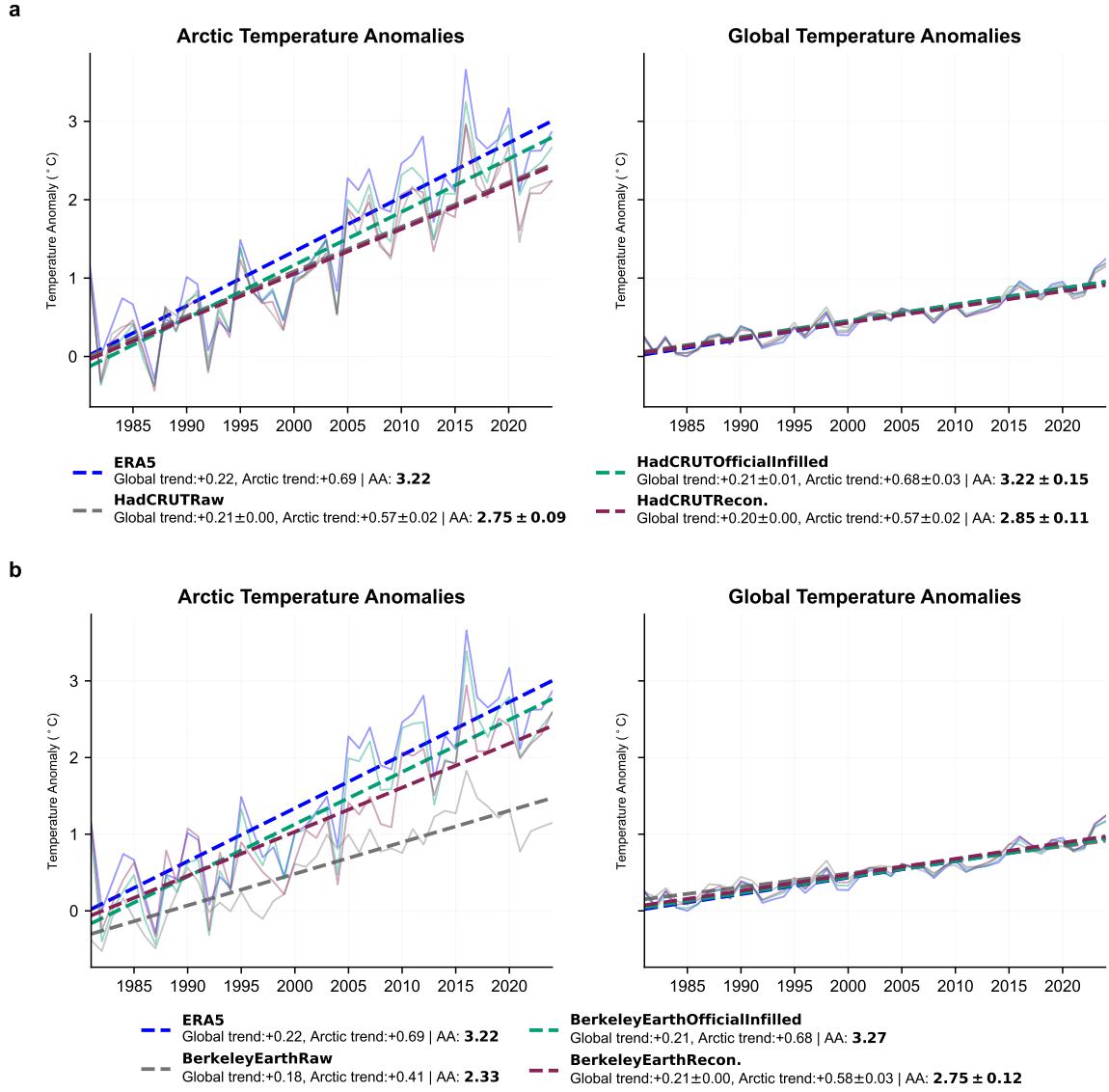


Fig. S23 Re-assessment of Arctic Amplification magnitude during the satellite era (1981–2024). Time series of annual mean surface temperature anomalies for the Arctic region (Lat $> 66.5^{\circ}\text{N}$, left column) and the globe (right column). **a**, Comparison using HadCRUT5 as the observational basis. Tracks show the evolution of anomalies derived from: ERA5 reanalysis (blue); sparse raw observations (grey); the official infilled product (green); and our generative reconstruction (purple). Straight dashed lines represent linear least-squares trends. The Arctic Amplification factor (AA), defined as the ratio of the Arctic warming trend to the global warming trend, is reported in the legend along with the trend magnitudes. Crucially, for the HadCRUT5-based reconstruction, this uncertainty explicitly propagates both the measurement uncertainty (derived by reconstructing each of the 200 HadCRUT5 observational ensemble members) and the model's epistemic uncertainty (derived from 5 independent DM-Fid realizations for each observational member). **b**, Similar comparison using Berkeley Earth as the observational basis.

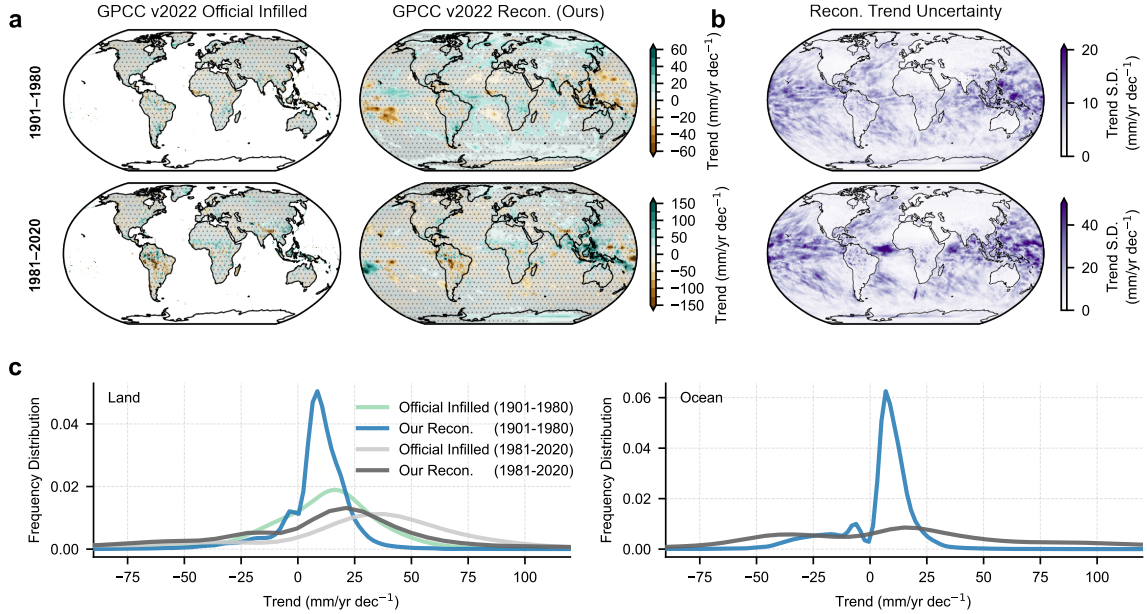


Fig. S24 Re-evaluating historical precipitation trends using the GPCC v2022. **a**, Global maps of linear precipitation trends ($\text{mm yr}^{-1} \text{dec}^{-1}$) comparing the official infilled GPCC v2022 product and our DM-Fid reconstruction (ensemble mean) during historical (1901–1980) and modern (1981–2020) periods. Regions with statistically non-significant trends ($p \geq 0.05$) are masked with gray shading and stippling. Statistical significance is assessed following an AR(1) adjustment after ref.[61] to account for serial correlation. For the official infilled product, the resulting p -values are subsequently adjusted using a False Discovery Rate (FDR) control [62]. For our reconstruction, the AR(1)-adjusted p -values from the ensemble members are combined using Fisher's method, followed by an FDR correction to strictly control for false discoveries. **b**, Uncertainty of the reconstructed precipitation trends, quantified as the standard deviation of the trend maps derived from the individual DM-Fid ensemble members. **c**, Frequency distribution of area-weighted statistically significant precipitation trends, estimated via Gaussian kernel density estimation (KDE). The distributions are separated into Land (where the reconstruction is constrained by gauge observations) and Ocean (where trends are inferred via learned teleconnections).

Supplementary Tables

Table S1 Quantitative benchmarking of reconstruction methods. Performance comparison across three resolutions (Temperature 5°, 1°; Precipitation 0.5°) on both ERA5 and CMIP6 test sets with a 95% missing data rate. Metrics (mean temporal correlation coefficient, TCC; mean normalized Root Mean Square Error, nRMSE) indicate that DM-Ens (mean of N=50) and DM-Fid (mean of N=5) consistently outperform statistical and deep learning-based benchmarks. Best results are highlighted in bold.

ERA5 test									
	Statistic Recon. ¹		LaMa Recon.		DM-Fid Recon. (Ours)		DM-Ens Recon. (Ours)		
	TCC (↑)	nRMSE (↓)	TCC (↑)	nRMSE (↓)	TCC (↑)	nRMSE (↓)	TCC (↑)	nRMSE (↓)	
Temp 5deg	0.55	0.77	0.58	0.70	0.76	0.59	0.77	0.59	
Temp 1deg	0.90	0.39	0.40	1.17	0.95	0.25	0.91	0.32	
Precip 0.5deg	0.86	0.53	0.05	1.66	0.90	0.46	0.91	0.44	
CMIP6 Test									
	Statistic Recon. ¹		LaMa Recon.		DM-Fid Recon. (Ours)		DM-Ens Recon. (Ours)		
	TCC (↑)	nRMSE (↓)	TCC (↑)	nRMSE (↓)	TCC (↑)	nRMSE (↓)	TCC (↑)	nRMSE (↓)	
Temp 5deg	0.58	0.75	0.63	0.69	0.81	0.55	0.78	0.54	
Temp 1deg	0.92	0.36	0.42	1.17	0.97	0.20	0.96	0.23	
Precip 0.5deg	0.91	0.43	0.05	1.60	0.95	0.30	0.96	0.29	

¹For temperature reconstruction, we used Kriging interpolation; for precipitation reconstruction, we used Angular Distance Weighting interpolation.

Table S2 Impact of physical pre-training on reconstruction fidelity. Quantitative sensitivity analysis comparing 5° temperature reconstruction (5% random observation) across different training configurations. Training solely on limited observational data (ERA5) results in poor generalization. In contrast, pre-training with climate model simulations significantly improves performance by providing a robust physical inductive bias.

Training data	ERA5 T2M Test		CMIP6 TAS Test	
	Mean TCC (\uparrow)	Mean nRMSE (\downarrow)	Mean TCC (\uparrow)	Mean nRMSE (\downarrow)
ERA5	0.58	0.64	0.61	0.65
CMIP6	0.75	0.58	0.81	0.53
CMIP6+ERA5	0.70	0.59	0.78	0.54

Table S3 Evaluation of warming trends (1981–2024) at high-latitude Arctic stations. The table compares linear warming trends (°C/decade) calculated from raw station observations (locations mapped in Fig. S22) against those extracted from official infilled products and our reconstruction. The analysis is stratified into two groups: Greenland-Barents stations (IDs 0–8; partially involved in Berkeley Earth, but have been supplemented here), where **bold red** values highlight the estimate closer to observations; and pan-Arctic reference stations (IDs 9–38; involved in Berkeley Earth), where **bold blue** values denote the closer estimate. The ‘Closer Match %’ quantifies the proportion of stations within each network subset where the specific method (official infilled products or our reconstruction) yields a lower absolute error relative to the observed trend.

ID	Coordinates	Station	HadCRUT5 Trend		Berkeley Earth Trend	
		Obs. (°C/dec)	Off. Inf. (°C/dec)	Our Recon. (°C/dec)	Off. Inf. (°C/dec)	Our Recon. (°C/dec)
Greenland-Barents Stations (Partially involved in Berkeley Earth)						
0	78.25°N, 15.50°E	1.167	0.673	0.886	0.840	0.869
1	76.51°N, 25.01°E	1.158	0.654	0.602	0.769	1.106
2	78.92°N, 11.93°E	0.966	0.540	0.644	0.941	0.970
3	74.50°N, 19.00°E	0.730	0.397	0.479	0.491	0.697
4	83.66°N, 33.37°W	1.010	0.802	0.530	0.704	0.976
5	68.71°N, 52.85°W	0.936	0.595	0.654	0.671	0.951
6	67.01°N, 50.72°W	0.685	0.595	0.654	0.654	0.455
7	76.77°N, 18.67°W	0.604	0.685	0.554	0.534	0.743
8	74.31°N, 20.22°W	0.450	0.537	0.459	0.503	0.425
Closer Match %			22%	78%	22%	78%
Pan-Arctic Reference Stations (Involved in Berkeley Earth)						
9	66.87°N, 162.63°W	0.474	0.590	0.499	0.494	0.476
10	66.54°N, 151.31°W	0.271	0.541	0.267	0.382	0.257
11	66.56°N, 25.84°E	0.539	0.478	0.534	0.502	0.690
12	68.62°N, 81.20°W	0.655	0.612	0.613	0.681	0.670
13	69.10°N, 105.12°W	0.668	0.591	0.627	0.599	0.703
14	70.39°N, 68.41°W	0.678	0.712	0.781	0.664	0.705
15	72.56°N, 77.78°W	0.711	0.732	0.654	0.691	0.711
16	66.53°N, 24.65°E	0.520	0.431	0.477	0.494	0.530
17	67.28°N, 28.18°E	0.577	0.478	0.534	0.507	0.577
18	67.37°N, 26.64°E	0.648	0.478	0.534	0.494	0.711
19	67.75°N, 29.61°E	0.504	0.478	0.534	0.514	0.584
20	67.82°N, 27.75°E	0.544	0.478	0.534	0.501	0.683
21	68.39°N, 27.42°E	0.346	0.478	0.534	0.470	0.475
22	68.85°N, 28.30°E	0.551	0.478	0.534	0.478	0.563
23	69.75°N, 27.00°E	0.554	0.478	0.534	0.451	0.470
24	68.15°N, 14.65°E	0.391	0.336	0.353	0.347	0.320
25	69.47°N, 25.51°E	0.545	0.478	0.534	0.444	0.512
26	69.57°N, 18.98°E	0.347	0.380	0.289	0.376	0.198
27	70.00°N, 23.26°E	0.400	0.378	0.359	0.394	0.279
28	66.51°N, 66.61°E	0.520	0.642	0.734	0.577	0.530
29	66.62°N, 72.91°E	0.555	0.648	0.612	0.596	0.554
30	66.62°N, 34.30°E	0.600	0.490	0.522	0.556	0.597
31	67.41°N, 78.70°E	0.702	0.645	0.735	0.631	0.701
32	67.63°N, 48.66°E	0.601	0.533	0.562	0.593	0.600
33	68.11°N, 164.15°E	0.823	0.696	0.758	0.772	0.823
34	72.31°N, 52.70°E	0.854	0.556	0.727	0.895	0.854
35	73.50°N, 80.23°E	0.912	0.867	0.877	0.746	0.911
36	67.83°N, 20.34°E	0.517	0.431	0.477	0.433	0.358
37	66.91°N, 151.61°W	0.257	0.541	0.267	0.382	0.257
38	71.36°N, 156.52°W	1.057	0.719	0.757	0.795	0.973
Closer Match %			23%	77%	30%	70%

Table S4 Hyperparameter configuration for generative diffusion models. Detailed settings for the three reconstruction models targeting different variables and resolutions. We employed a Video U-Net architecture within a Variance Exploding SDE (VE-SDE) framework. Hyperparameters were adjusted to accommodate the varying spatial resolutions and physical statistical properties of temperature versus precipitation fields. Inference guidance weights ($\lambda_{obs}, \lambda_{temp}$) were optimized via iterative zoom search to balance observation fidelity and temporal consistency.

	Temp (5°)	Temp (1°)	Precip (0.5°)
<i>Input & Optimization</i>			
Input Resolution ($H \times W$)	36 \times 72	180 \times 360	360 \times 720
Sequence Length (Frames)	12	12	6
Batch Size	128	8	8
Learning Rate	5×10^{-4}	2×10^{-4}	2×10^{-4}
Dropout	0.15	0.15	0.15
EMA Rate	0.9999	0.9999	0.9999
Optimizer	Adam	Adam	Adam
<i>Diffusion Process (VE-SDE)</i>			
σ_{min}	0.01	0.01	0.03
σ_{max}	15.0	15.0	15.0
Sampling Steps	100 (DM-Ens); 1000 (DM-Fid)	250 (DM-Ens); 1000 (DM-Fid)	250 (DM-Ens); 1000 (DM-Fid)
<i>Network Architecture (Video U-Net)</i>			
Base Channels	32	32	32
Channel Multipliers	(1, 2, 4)	(1, 2, 4)	(1, 2, 4, 8)
Res. Blocks per Scale	2	2	2
Num. Heads	1	1	1
<i>Inference Guidance (DM-Ens / DM-Fid)</i>			
λ_{obs}	0.43 / 0.07	0.28 / 0.23	0.12 / 0.12
λ_{temp}	7.4×10^{-4} / 1.1×10^{-4}	7.1×10^{-4} / 5.7×10^{-4}	5.9×10^{-4} / 5.5×10^{-4}